PCCP

Accepted Manuscript

ROYAL SOCIETY OF CHEMISTRY

www.rsc.org/pccp

A Detailed Study of Cholinium Chloride and Levulinic Acid Deep Eutectic Solvent System for CO_2 Capture via Experimental and Molecular Simulation Approaches

Ruh Ullah,[a] Mert Atilhan,[a*] Baraa Anaya,[a] Gregorio García,[b] Ahmed ElKhattat,[a] Mohammad Tariq,[a] and Santiago Aparicio[b*]

[a] Department of Chemical Engineering, Qatar University, P.O. Box 2713, Doha, Qatar
[b]Department of Chemistry, University of Burgos, 09001 Burgos, Spain

[*]Corresponding authors: mert.atilhan@qu.edu.qa (M. A.) andsapar@ubu.es (S. A.)

Abstract.

Choline chloride + levulinic acid deep eutectic solvent is studied as a suitable material for CO_2 capturing purposes. The most relevant physicochemical properties of this solvent are reported together with the CO_2 solubility as a function of temperature. The corrosivity of this solvent is studied showing better performance than amine-based solvents. A theoretical study using both Density Functional Theory and Molecular Dynamics approaches is carried out to analyze the properties of this fluid from the nanoscopic viewpoint and their relationship with the macroscopic behavior of the system and its ability for CO_2 capturing. The behavior of liquid – gas interface is also studied and its role on the CO_2 absorption mechanism is analyzed. The combined experimental plus theoretical reported approach leads to a complete picture of the behavior of this new sorbent with regard to CO_2, which together with its low pricing, and the suitable environmental and toxicological properties of this solvent, lead to a promising candidate for CO_2 capturing technological applications.

Keywords: Deep eutectic solvents; carbon capture; thermodynamics; molecular simulations.

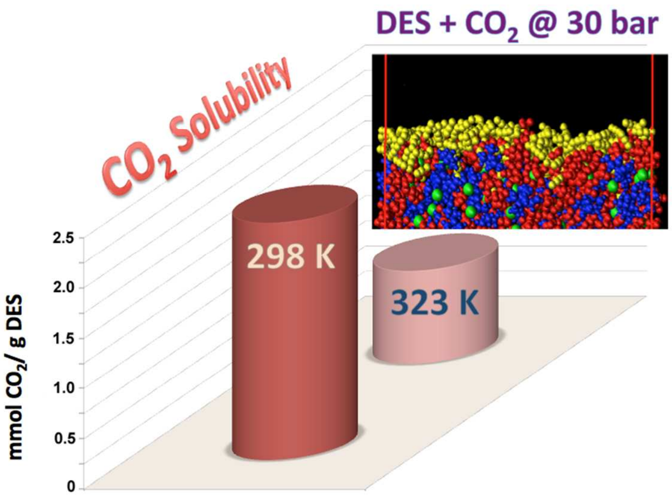

Graphical Table of Content

1. Introduction

Carbon dioxide capture is one of the most relevant technological,[1]environmental,[2] social[3] and economic[4] needs nowadays. The effect of anthropogenic CO_2 atmospheric emissions on global warming has been widely proven,[5,6] which in all the considered scenarios will lead to increasing temperatures at a global level,[7] with large economic, social and environmental consequences.[8,9] The most important source of anthropogenic CO_2 emissions rises from fossil fuels combustion for transportation, power generation and industrial purposes.[10,11,12]In particular, electricity production from fossil fuelled power plants takes account of a large percentage of total CO_2anthropogenic emissions,[13,14] and thus, reducing these emissions has a pivotal role for controlling climate change. In spite of the remarkable advances in renewable electricity production approaches, the state-of-the-art of these methods is not alternative to fossil fuels, and thus, all the projections show that power plants based on fossil fuels would develop a pivotal role for energy production along the next decades.[15,16] Therefore, a realistic approach for reducing CO_2 emissions in a reasonable timeframe is to develop suitable technologies that allow for capturing CO_2 from flue gases in fossil fuelled power plants.[17,18,19,20,21,22]

The state-of-the-art of CO_2 capture technologies does not allow carbon capturing without an unacceptable increase in the costs of electricity generation,[23,24,25] which hinders their application for the required large scale. The most common approach for carbon capturing is post-combustion sorption based on alkanolamine liquid sorbents,[26,27] which although showing large affinity for CO_2 molecules has serious technological drawbacks, such as facilitates corrosion, solvent evaporation or degradation, and large capturing costs.[23,28,29,30,31.32,33,34,35] Therefore, alternative CO_2 sorbents have been studied in the last few years such as metal-organic frameworks,[36] solid sorbents,[37] carbon-based materials,[38] or membranes.[39]One alternative that has attracted great attention are ionic liquids, IL,[40, 41,42] because of the possibility of tuning their properties, and thus their affinity for CO_2 molecules, through the selection of suitable ions. Nevertheless, ILs have also showed some problems with regard to their application for carbon capture purposes such as their large viscosity or their cost, which have hindered their application for capturing purposes at industrial scale.[43,44,45,46,47,48] Therefore, although these drawbacks should not be considered as a motive for discarding ILs as possible CO_2 capturing candidates,[49,50,51,52]several alternatives have been proposed to maintain the design flexibility of ILs while avoiding their well-known problems. Deep eutectic solvents (DES) are among the most promising options to overcome these IL problems while maintaining their positive properties and the ability of tuning their behavior.[53,54] DES are usually a binary mixture of a salt (or IL) with an hydrogen bond donor (HBD), which at a certain molar ratio leads to a system with a melting point close to ambient temperature and lower than those for the pure compounds generating the DES.[53,54,] Although several salts have been proposed for developing DES, most of the available literature is based on cholinium chloride ([CH][Cl]) (Figure 1).[54] [CH][Cl] is a non-toxic and biodegradable compound; and it can be obtained at very low cost.[55,56] [CH][Cl] may lead to DES when mixed with different types of HBDs such as urea, polyols (glycerol or ethylene glycol), sugars or carboxylic acids. To maintain the suitable characteristics of [CH][Cl] when developing DES, this salt has to be combined with suitable HBDs, and thus, an approach is using HBDs.[57,58] In recent works Maugeri et al.[59] and Florindo et al.[60] proposed the use of HBDs combined with [CH][Cl]. Levulinic acid ([LEV]) is a compound fully biodegradable, non-toxic, that may be obtained from biomass at low costs,[61,62,63] and thus [CH][Cl] + [LEV] DES (Figure 1.) may be considered as a renewable materials. [CH][Cl] + [LEV] lead to DES when mixed ([CH][Cl] : [LEV] at 1:2 molar ratio, CHCl_LEV_1_2).[59,60] The available studies on CO_2 capture using [CH][Cl] based DES are mostly limited to systems containing HBDs such as urea, glycerol, ethyleneglycol or carboxylic acids such as malonic or lactic,[64,65,66,67,68,69,70,71,72] but no studies for DES involving [LEV] are reported. Therefore, a study on the suitability of CHCl_LEV_1_2 DES for CO_2 capturing purposes is reported in this work. Considering that a full characterization of this material is required for analyzing their weaknesses and strengths for carbon capture purposes, a physicochemical characterization of CHCl_LEV_1_2 was carried out, in which the most remarkable properties were selected both because they are required for process design purposes and/or because they provide information about the structure and behavior of the fluid. CO_2 absorption was studied at isothermal conditions pressures up to 30 bar. Likewise, in order to understand the mechanism of CO_2 absorption at a nanoscopic level, a theoretical study using both molecular dynamics, MD, and quantum chemistry (in the Density Functional Theory, DFT, framework) approaches was reported. The fluid's structure was studied for pure CHCl_LEV_1_2 and for this fluid after CO_2 absorption as a function of temperature, pressure and amount of absorbed CO_2 via MD simulations. Short-range interactions in the fluid were analyzed in detail from DFT calculations. Likewise, considering the relevance of liquid – gas interfacial behavior for CO_2 capturing purposes, MD simulations were also carried out for analyzing the behavior of CO_2 molecules at the DES surface. The reported study shows for the first time a combined full experimental and computational characterization of DES as sorbents for CO_2 capturing purposes.

2. Methods

2.1 Materials

Levulinic acid (CAS:123762, Aldrich) and choline chloride (CAS: 67481, Iolitec) were used as received. A mixture of 1:2 molar ratio of [CH][Cl]:[LEV] acid (CH_Cl_LEV_1_2 DES) was prepared by mixing 46.54 g of chlorine chloride and 77.41 g of [LEV]. The resulting mixture was stirred for 2 hours using a magnetic stirrer. The formation of eutectic solution was examined and confirmed using both NMR (Varian Unity Inova 400 MHz) and FTIR spectrometer (Spectrum 400, PerkinElmer, USA). CH_Cl_LEV_1_2 DES sample is prepared by mixing the ionic liquid and acid at room temperature in a glove box compartment. Water content (1.69 wt %) was measured using Karl Fischer coulometric titration (Metrohm 831 KF coulometer) to 0.3% accuracy in water mass content.

2.2 Experimental details

NMR measurements were done using a Varian Unity Inova 400 MHz equipment at 298.15 K (± 0.1 K) for the ^{1}H and ^{13}C nuclei. CHCl_LEV_1_2 samples were prepared on 5 mm NMR tubes, with 0.005 g of CHCl_LEV_1_2 mixed with 1 mL of D_2O.

The formation of DES was examined and confirmed using the FTIR spectrometer, Spectrum 400, PerkinElmer, USA. Other than the FTIR studies for characterization of the DES system, in-situ FT-IR measurements were carried out by using Bruker® Vertex 80 Fourier transform infrared spectrometer, which is coupled with temperature controlled high pressure liquid cell (HPL-TC) that can go up to 30 bars and supplied by Harrick^{TM} Scientific. HPL-TC was equipped with high-resolution Si windows, teflon spacers of 2280 micron path-length and Viton® o-rings. The path-length was intentionally kept long to provide more volume, and therefore increase the contact opportunity between CO_2. In order to adjust CO_2 pressure a gas feeding manifold system was designed and the schematics are shown in Figure S1.

Density and viscosity were both measured through an Anton Paar DMA 4500M and Lovis 200 M/ME units respectively. The density meter uses the oscillating U-tube sensor principle and it has a volume requirement of 1 mL of sample. The density meter has the accuracy of density measurement reported as 0.00005 g/m^3 in density and ± 0.05 K in temperature. Anton Paar Lovis 200 rolling ball viscometer measures the rolling time of a ball through transparent and opaque liquids according to Hoeppler's falling ball principle with ± 3 % viscosity uncertainty and ± 0.02 K accuracy in temperature measurements.

The pH and conductivity measurements were performed at 293.15 K by pH/conductivity meter (3200M Multi-parameter Analyzer, Agilent Technologies, USA). The conductivity and the pH of the final product was 752.85 ± 5.2 μs/cm and 2.7 ± 0.2 at temperature of 293.15 K. Indeed, conductivity is an important indicating property, where IL can play the role of both solvents and electrolytes in electrochemical reactions. Ionic liquids exhibit a broad range of conductivities from 0.1 to 20 mS cm^{-1} as conductivity is affected by many factors such as density, viscosity, anionic charge, ion size, delocalization, aggregations and ionic motions.[73] Recently, some DES liquid systems based on choline chloride,[74] with properties similar to those of ionic liquids, have been prepared by mechanically mixing two different components, where choline can be used as alternative cation in combination with suitable anion to generate ionic liquids.

Refractive Index with regard to the sodium D-line were measured ($\pm 1\times 10^{-5}$) using an automated Leica AR600 refractometer, with the sample temperature being controlled using a Julabo F25 external circulator and measured with a built-in thermometer (±0.01 K). A standard supplied by the manufacturer was used for refractometer calibration.

Corrosion experiments were conducted using circular specimens of carbon steel 1018 (0.186 wt% C, 0.214 wt% Si,0.418 wt% Mn, 0.029 wt% P, 0.019 wt% S, balance Fe) with 1.93 cm^2 surface area of specimen exposed to the medium. Carbon steel 1018 is selected for corrosion experiments since it is a common material that is used in process equipment in chemical industries. The specimens were prepared according to ASTM G1-03 standard by wet grinding and polishing using 320,600 and 1200 grit SiC papers. The specimen was then degreased by high purity acetone, rinsed with deionized water and dried with hot dry air.[75] Electrochemical experiments were conducted in 100 cm^3 jacketed micro cell supplied by Autolab (Figure 2). The microcell was equipped with a potentiostat (Autolab PGSTAT101) and data acquisition system (NOVEA 1.7). The corrosion cell consisted of Ag/AgCl reference electrode filled with 3M KCl solution, two 316 stainless steel counter electrodes and the working electrode. Heated water circulator was connected to the outer cell jacket throughout experiments for temperature control. Water-cooled condenser was utilized to minimize vaporization losses of the test solution. Gas supply streams and CO_2 gas flow meter was connected to the cell. Throughout all experiments, a gas stream was maintained in the gas phase of the cell. Open circuit potential OCP measurement of the specimen against the reference electrode was recorded until it is stable (defined as ± 0.01 mV between successive readings). The polarization curve was generated directly by the data acquisition system in the range of ±250 mV vs OCP and a scan rate of 0.001 V/sec. Tafel extrapolation method was used to determine corrosion current (Icorr) which was converted to corrosion rate by the following equation:

$$CR = \frac{3.27\times10^{-3}\times I_{corr}\times EW}{\rho} \quad (1)$$

where CR is corrosion rate in (mm/yr) , I_{corr} is corrosion current in (μA/cm^2) , EW is the equivalent weight of the carbon steel specimen (g/equivalent) and ρ is the density of the specimen (g/cm^3). The numerical value that appears in equation 1 is a constant that defines the units for the corrosion rate and it is calculated from the calibration of the apparatus.

Thermal stability analysis of materials was performed with Perkin Elmer Pyris 6 TGA instrument, where, samples were heated in N_2 environment from 303 K to 873 K at the rate of 5/min.

For carbon dioxide adsorption measurements, a high-pressure magnetic suspension sorption apparatus (MSA) made by Rubotherm Präzisionsmesstechnik GmbH were used. Schematic of the apparatus is given in Figure S2. MSA apparatus is rated up to 350 bars at 373 K. MSA has two different operation positions. First, the measurement cell is filled with CO_2 gas, and MSA records the weight change of the sample that is placed in the sample container as the high-pressure gas is absorbed by the sample. The second measurement position is used to measure the in-situ density of the high-pressure gas, which is required to calculate the amount of the adsorbed gas onto the sample in the high-pressure cell. In this work, pressures up to 30 bars is used as the maximum pressure and at the end of each isotherm, hysteresis check is conducted at each isotherm by collecting desorption data as the system is depressurized. Physical adsorption nature is later is cross-checked by comparing before and after FTIR measurements of the DES sorbent. CO_2 adsorption-desorption isotherms were selected as 298.15 K and 323.15 K. Detailed operating principles and data correlation of the magnetic suspension force transmission is also discussed previously elsewhere.[76,77]

For buoyancy calculations used in sorption measurements, in-situ density of the pressurized gas in the high-pressure cell is measured. Archimedes' principle is used for density measurements by utilizing a calibrated silicon sinker placed just above the sample basket in the pressure cell. The silicon sinker used in this apparatus had a volume of 4.4474 cm^3 measured at 20 ^{0}C with a 0.0015 cm^3 uncertainty and a density of 4508 kg/m^3 measured at 293.15 K with a 4 kg/m^3 uncertainty. On the other hand, the uncertainty for pressure measurements is ±0.05% in full scale of the 350 bar rated pressure transducer and ±0.1 K for the temperature measurements.

2.3 Simulations

Optimizations from those systems composed by one isolated molecule (*i.e.* ions, levulinic acid or CO_2) up to systems composed by DES and CO_2 (CHCl_LEV_1_2···CO_2) were optimized. Optimized minima were checked trough their vibrational frequencies. For those simulations wherein two or more molecules are present, different starting points were employed in order to study different relative dispositions, focusing our attention on the disposition of minimal energy. All these calculations were carried out using B3LYP[78,79] coupled with dispersion corrections according to Grimme's scheme[80] (B3LYP-D2), with 6-31+G** basis set. B3LYP has been selected since it has showed a remarkable performance over a wide range of systems,[81] while dispersion corrections are adequate since we are considering systems with dispersive interactions such as hydrogen bonds.[80] Besides, calculated energies after dispersion corrections are comparable with more reliable values, such as those obtained at MP2 level.[82]

From those systems composed by two or more molecules, computed energies were corrected (to avoid basis set superposition error) according to counterpoise procedure.[83]Interaction energies (ΔE) for different process related with CO_2 capture and formation of DES were computed. Thus, ΔE for CHCl_LEV_1_2···CO_2 (*i.e.* CO_2 capture using DES) was calculated as: $\Delta E_{DES\cdot CO2} = E_{DES\cdot CO2} - (E_{DES} + E_{CO2})$, being $E_{DES\text{-}CO2}$, E_{DES} and E_{CO2} the (counterpoise corrected) energies for CHCl_LEV_1_2···CO_2, CHCl_LEV_1_2 and CO_2, respectively. Intermolecular interactions were analyzed by means of Atoms in Molecules (AIM) theory.[84] Topological analyses according AIM theory were carried out using MultiWFN package.[85] According to Bader's theory,[84] there are four kinds of critical points, but giving the characteristics of the studied systems and to improve and clarify data analysis we have mainly focused over bond critical points (BCP), which raises the criteria for considering the presence of intermolecular interactions. Finally, atomic charges were computed to fit the electrostatic potential according to the ChelpG scheme.[86] All calculations were carried out with Gaussian 09 (Revision D.01) package.[87]

MD simulations were carried both for pure CHCl_LEV_1_2 and for CHCl_LEV_1_2 + CO_2 systems. In the case of pure DES, 250 [CH][Cl] ion pairs plus 500 [LEV] molecules were considered for all the simulations in the 298 to 348 K temperature range at 0.1 MPa of pressure. Mixed CHCl_LEV_1_2 + CO_2 were prepared according to the experimental solubility data obtained in this work, and thus, four different mixed systems were prepared for simulations at 298 K, all of them containing the same number of ion pairs an [LEV] molecules as for pure DES simulations and with different number of CO_2 molecules to mimic experimental adsorption isotherm up to 1 MPa (samples CHCl_LEV_1_2_CO_2_I, CHCl_LEV_1_2_CO_2_II, CHCl_LEV_1_2_CO_2_III, and CHCl_LEV_1_2_CO_2_IV; Table S2, ESI). All these simulations were carried out in the NPT ensemble, with initial low density boxes (~ 0.2 g×cm^{-3}) built using the Packmol program.[88] Simulations were carried out starting from these initial boxes being equilibrated during 5 ns with additional 10 ns runs collected for production purposes.

In the case of MD simulation for the analysis of interfacial behavior, a box of CHCl_LEV_1_2 with the same characteristics of those used for the simulation of pure DES, and previously equilibrated, was put in contact along the z-direction with *i*) a vacuum layer (with the vacuum layer dimension in the z-coordinate three-times larger than the DES layer) for describing the DES – vacuum interface, and *ii*) with a CO_2 gas phase (with gas layer also being three-times larger in the z-dimension than the DES liquid layer) for considering DES – CO_2 gas interface. The density of the CO_2 gas layer correspond to that at 298.15 K and 10 bar obtained from CO_2 reference equations of state.[89] These interfacial simulations were carried out in the NVT ensemble at 298.15 K.

All the MD simulations were carried out using the MDynaMix v.5.2 molecular modeling package.[90] Pressure and temperature were controlled using the Nose–Hoover thermostat. Coulombic interactions were handled with the Ewald summation method,[91] with cut-off radius of 15 Å. Tuckerman–Berne double time step algorithm,[92] with long and short time steps of 1 and 0.1 fs, was considered for solving the equations of motion. Lorentz-Berthelot mixing rules were used for Lennard-Jones terms.

The forcefield parameterization used along MD simulations is reported in Table S1 (Electronic Supplementary Information, ESI). This parameterization was developed using DFT calculations for clusters formed by 1 [CH][Cl] + 2 [LEV] molecules which were optimized as reported in previous section, and thus, ChelpG[86] charges were calculated for this cluster. The optimized structures for this model cluster show that LEV molecules may interact in two different positions (see Results and Discussion Section), with [LEV] molecules having different charges depending on the interacting site. Therefore, the used parameterization considers two types of levulinic acid molecules (LEV_I and LEV_II) with different charge parameters (Table S1, ESI). The proposed parametrization leads to charges of +0.8254 for $[CH]^+$, -0.6849 for Cl^-, -0.0663 for LEV_I, and -0.0743 for LEV_II. This parameterization was developed to obtain a more realistic physical picture of the charge distribution in the studied DES instead of applying the simplified option of +/- 1 total charge for the cation/anion and null charges for any LEV molecule.

3. Results and discussion

3.1 Density, refraction index and viscosity

These properties were collected, Table S3 (ESI) and presented in Figure 3. Similar DES systems have been studied and their density and viscosity profiles have been reported for CHCl and levulinic acid,[60] glyceric acid,[60] phenol,[93] urea,[94] and glycerol[95] containing DES systems elsewhere. Density and viscosity values are important for these exotic mixtures for development of suitable equations of state, which has a crucial role in calculation of further thermodynamic properties for developing industrial processes including gas separation operations that runs with novel solvents substitutes of amines. Most of the studied DES system densities are in the range of 1 – 1.35 gcm^{-3} at 25 °C. DES systems that contain metallic salts show tendency to have higher densities at room temperature in the range of 1.3 – 1.6 g/cm^{3}. [CH][Cl] and urea DES systems (with 1:2 ratio) have been reported to have 1.25 g cm^{-3} density at 293.15 K.[96] For the experimented CHCl_LEV_1_2 DES system, density values falls in the range of 1.14 – 1.10 g cm^{-3} between temperature range of 293.15 K to 363.15 K. This shows a similarity of the values of a similar DES system formed with [CH][Cl] and a different acid based HBD. Refractive index follow a linear trend in the 298.15 K to 238.15 K range with values in the 1.466 to 1.455 range. These refractive index values are in the lower range for the DES studied in the literature, nevertheless they show that CHCl_LEV_1_2 DES is a highly polarizable solvent.[96]

On the other hand, viscosity has also been extensively measured for the available DES, due to its importance for industrial purposes. Viscosity data are required for DES applications not only in gas solubility and separation processes but also in fields such as lubrication or any other potential high-pressure operation have been considered as well.[97] Moreover, viscosity data is essential to realize the possible mass transfer coefficient limitations as well as fluid pumping issues for advanced process system and equipment design purposes. [CH][Cl] couple with various HBD DES systems have recently been investigated and their viscosities have been reported and quite high viscosity values have been observed. For [CH][Cl] and urea 1 to 2 DES system viscosity of 750 mPa×s at 298.15 K has been reported.[94] Moreover, again for [CH][Cl] and glycerol,[95] ethylene glycol,[94] glycolic acid,[60] and phenol[93] DES systems, viscosity values of 246.8, 35, 394.8 and 35.1 mPa×s at 303.15 K have been observed respectively. For the experimented CHCl_LEV_1_2 DES system, viscosity at of 171.3 mPa×s at 298.15 K has been observed in this work. Florindo et al.[60] also reported a viscosity value of a same system for temperatures between 298.15 K and 350 K (e.g. 226.8 mPa×s at 298.15 K).

The difference between viscosity data reported in this work and those by Florindo et al.[60] rises from i) the different methodology for sample preparation (grinding, Florindo et al.,[60] or mixing, this work, DES components), and ii) the different water content. The most remarkable feature should be the water content, which develops a pivotal role for viscosity measurements. The sample used in this work has a water content of 1.6 wt % which is higher than the 0.23 wt % of the sample used by Florindo et al.,[60] which would justify the lower viscosity data reported in this work, Figure 3b. This is confirmed by the viscosity data reported by Florindo et al.[60] for CHCl_LEV_1_2 DES saturated with water (9.88 wt %), which shows less viscous behavior than the sample used in this work.

3.2 NMR and FTIR

^{1}H and ^{13}C NMR features are summarized in Table S4 (ESI), the data are in good agreement with those by Florindo et al.[60] and it discards the presence of relevant impurities at least at the NMR detection levels. FTIR characterization of the DES structure provides information about interactions and complexation between constituents. FTIR spectra of pure [LEV] and choline chloride are given in Figure S1 (ESI). Regarding pure [LEV], vibrational bands at 1720-1695 cm^{-1}, 1435-1400 cm^{-1}, 1380-1345 cm^{-1} and 1225-1100 cm^{-1} refers to the presence of aliphatic ketone, while the vibrational bands 1720-1701 cm^{-1} refers to a carbonyl compound. The FTIR spectrum of the [LEV] confirms its classification as a keto-acid. For pure choline chloride, vibrational bands at 3540-3200 cm^{-1} and 1205-885 cm^{-1} refers to the presence of hydroxyl or amino group, while those bands at 2990-2855 cm^{-1} and 1485-1415 cm^{-1} refers to the presence of an alkyl group cm^{-1}. On the other hand, the formation of formation of DES was confirmed from by the FTIR spectrum of CHCl_LEV_1_2 DES 1:2 molar ratio as shown in Figure 4, where, the vibrational bands at 2990-2855 cm^{-1} and 1485-1415 cm^{-1} indicate the presence of alkyl group, 1720-1695 cm^{-1} bands, 1435-1400 cm^{-1}, 1380-1345 cm^{-1} and 1225-1100 cm^{-1} bands represent the aliphatic ketone group, 1720-1701 cm^{-1} bands refer to a carbonyl compound, and 1745-1710 and 1300-1000 cm^{-1} bands refer to an ester or ketone compound.

3.3 In-situ FTIR

For in-situ FT-IR measurements temperature controlled high-pressure liquid cell (HPL-TC) manufactured by Harrick Scientific was used. HPL-TC was equipped with specific internal parts: high-resolution Si windows, Teflon^{TM} spacers of 2280-micron path-length and Viton O-rings. The path-length was intentionally kept thick to provide more volume, and therefore increase the contact opportunity between CO_2 and the solvent molecules as well as to provide a more stable sealed system. In order to manipulate CO_2 injection at the desired pressures under isothermal condition, a particular system was designed and attached to the spectrometer. In-situ FTIR experiment was performed under 50 ºC over a range of low CO_2 pressures. To ensure thermal stability, the thermo-regulator was kept operating for at least one hour prior to the experiment. A background spectrum of the HPL-TC system under vacuum is collected before and after each DES in-situ FTIR measurement and this background is subtracted from the DES+CO_2 spectrum data. To this end, the sample spectrum was collected upon exposure to CO_2. This sample spectrum is believed to be influenced by the contribution of both CO_2 in the absorbed phase (dissolved in DES) and gaseous CO_2 in the bulk especially that the path-length is thick. Hence, in order to eliminate the gaseous CO_2 contribution, pure CO_2 spectra were collected separately at same conditions of the sample spectrum, and then each was subtracted from the sample spectrum that corresponds to same operating conditions. In-situ FTIR experimental findings of CHCL_LEV_1_2 DES with the presence of pressurized CO2 at different pressures are shown in Figure S3 (ESI). Near CO_2 fundamental bending mode (600-700 cm^{-1}), interesting gradual bands appear around 619 cm^{-1} analogous to the red-shifted bending mode band observed in the computational results which was overlapping with other CO_2-free DES and CO_2-loaded DES bands. The subtraction of gaseous CO_2 and DES spectra resulted in a loss of CO_2 related bands that are overlapped and appear as negative split bands. Nevertheless, the effect of the increasing pressure was observed and recognized by the increase in intensity that is corresponding to the increase in the concentration of absorbed CO_2 in liquid DES phase.

3.4 TGA

Thermal gravimetric analysis (TGA) of the DES system has been checked to see the temperature limitation of the absorbent. Figure 5 shows the TGA profile of the experimented DES system. Single step degradation behavior was observed and the analysis shows that the DES system is stable up to 453 to 473 °C, which makes the experimented DES system suitable for high temperature post combustion CO_2 capture process conditions as well.

3.5 Corrosion Measurements

Needless to say that corrosivity is one of the most important concerns in process operation point of view to forecast the equipment depreciation with time and make plans for not only during material selection for equipment design but also during the operation by selection the appropriate corrosion inhibitors to prevent the potential corrosion within the pipe and absorption column vessel. For this purpose, corrosion experiments have been conducted for the DES system and monoethanolamine (MEA) system, as it is the most widely used CO_2 capture agent in chemical plants. Figure 6 shows the current density vs potential plot for the two studied DES and MEA systems. The details on how to interpret the polarization curve are given in section 2.2 of this work. Two identical carbon steel samples are used for the corrosion experiments and they were prepared for the measurements as per ASTM G1-03 standards as mentioned in above section. The surface area of the specimens was calculated as 1.93 cm^2. The analysis on the polarization curves for the CO_2 loaded DES system showed that the corrosion potential is -0.43 V and the corresponding corrosion rate behavior is 0.027 mm/year. On the other hand, the corrosion behavior of the identical carbon steel specimen in CO_2 loaded MEA solution was conducted. Corrosion potential was recorded as -0.75 V and the corresponding corrosion rate was calculated as 0.54 mm/year. The results shows that from corrosion point of view the DES system exhibits much more corrosion resistant behavior when compared with MEA system and this considerable order of magnitude difference is a great advantage in reducing the both operating and fixed cost of the absorber column and its ancillary equipment in a CO_2 capture plant.

3.6 CO_2 Solubility

CO_2 solubility studies were conducted by using state of the art magnetic suspension based MSA and the details of the apparatus mentioned above. Pressure transducers (Paroscientific, US) were used in a range from vacuum up to 35 MPa with an accuracy of 0.01% in full scale. The temperature was kept constant with an accuracy of ± 0.5 K for each measurement (Minco PRT, US). In situ density values for CO_2 are measured during sorption measurements as it is necessary to calculate the absorbed CO_2 amount, and density values are cross-checked with REFPROP 9.0[98] for consistency purposes. Absorption measurements were carried out using 2 to 3 mL DES samples. First the system is taken under vacuum for 8 hours at 293 K, 298 K, 308 K, 318 K and 323 K. CO_2 is then pressurized through Teledyne Isco 260D fully automated compressor and fed into the high-pressure measurement cell in which the CO_2 absorption process begins. Once the solubility equilibrium is reached measurements are taken for a period of 10 minutes; each data point is collected at every 30 seconds. At the end of each measured pressure point, gas-dosing system triggers the compressor to the next pressure measurement point, which increases the measurement cell pressure in a step-wise manner. In this work, pressure up to 3 MPa (30 bars) is used for maximum pressure and 293 K, 298 K, 308 K, 318 K and 323 K isotherms were investigated for CO_2 absorption in DES system.

Solubility hysteresis check was conducted at each isotherm by collecting desorption data as the system is depressurized. Details of the solubility experiment is based on the amount of absorbed carbon dioxide on the sample is calculated by using below equation:

$$W + W_{buoy,sample} + W_{buoy,sink} = m_{abs} + m_{sample} + m_{sink} \qquad (2)$$

where;

W = signal read by the instrument

$W_{buoy,sample} = V_{sample} \times d_{gas}$ = buoyancy correction due to sample

V_{sample} = volume of the sample

d_{gas} = density of the gas

$W_{buoy,sink} = V_{sinker} \times d_{gas}$ = buoyancy correction due to sinker

V_{sinker} = volume of the sinker

m_{ads} = absorption amount

m_{sample} = mass of the sample

m_{sink} = mass of the sinker (sinker is a float that is used for in-situ gas density measurements)

Figure 7 shows the findings of the solubility measurements at 5 different isotherms up to 30 bars. It was observed that the maximum amount of CO_2 solubility was decreased with the increase in temperature. The DES system absorbed 2.316, 2.220, 2.100, 2.027 and 1.934 mmol of CO_2 per gram of DES sample at 293 K, 298 K, 308 K, 318 K and 323 K respectively at maximum operating pressure of 30 bar. Direct weight measurement technique allows in situ observation of the behavior of the measured sample. In other words, potential swelling effect can be observed during the measurements. In case of swelling of the sample, the increased sample volume would cause loss in the buoyancy on the measurement cell, which in turn would be obvious to see decrease in the amount of captured CO_2. However, as it can be seen from Figure 7 that the CO_2 absorption trend has been reported as a curve with a positive curvature. During the solubility measurements, sorption hysteresis was also checked by conducting absorption/desorption cycle analysis and none of measurements at each isotherm did not show a sign of chemisorption and weight measurements were obtained during the desorption along with the same absorption path. Moreover, in order to check whether there is a degradation of the sorption activity with the experimented DES system, each isotherm measurements were repeated three times and there was no significant absorption activity loss observed.

On the other hand, the kinetics of the absorption on DES system has been investigated. Figure 8 shows the amount of absorbed CO_2 in DES system with time at both low and high pressures. At 1 bar pressures average of 7 minutes were required reaching the equilibrium for a fully saturated DES solution. Whereas at 30 bars, 12 minutes passed to reach the equilibrium conditions.

3.7 Nanoscopic behavior from Molecular Dynamics

Forcefield parameterization used in this work was validated through the comparison of predicted physical properties with experimental values. Deviation between experimental and simulated density, ρ, data in the 298 to 348 K range are reported in Figure 9 Density data from MD are slightly lower than experimental data, but being closer to those by Florindo et al.[60] Nevertheless, deviations are lower than 0.9 % in the whole temperature range, which show the suitable performance of the used parameterization for describing macroscopic properties of the studied system. The temperature evolution of density, both for experimental and molecular dynamics predicted data, allows obtaining isobaric thermal expansion coefficient, α_p, from its thermodynamic definition, leading to 0.583×10^{-3}, 0.576×10^{-3} and $0.593\times10^{-3}\,K^{-1}$ at 298 K, for the experimental data obtained in this work, from Florindo et al.,[60] and from molecular dynamics simulations, respectively, which show excellent agreement for the simulated data with experimental values.

Self-diffusion coefficients were also calculated, using Einstein's equation from mean square displacements (msd), for all the involved molecules leading to values of 0.42×10^{-11} ($[CH]^+$), 0.68×10^{-11} ($[Cl]^-$), and 0.63×10^{-11} ([LEV]) $m^2\times s^{-1}$, at 298 K. The absence of experimental data hinders the comparison of simulated self-diffusion coefficients data; nevertheless, $[CH]^+$ cation moves slower than $[Cl]^-$ and [LEV], which show similar mobilities at 298 K. Perkins et al.[99] reported self-diffusion data from molecular dynamics simulations of reline DES (composed of [CH][Cl]+urea in 1:2 molar ratio), their values are lower than those obtained in this work for CHCL_LEV_1_2 (roughly the half) in agreement with the larger viscosity of reline in comparison with CHCL_LEV_1_2. Likewise, self-diffusion for $[CH]^+$ in reline are lower than for Cl^- and the corresponding HBD (urea), which is also in agreement with values for CHCL_LEV_1_2, but HBD in reline has larger molecular mobilities than that of $[Cl]^-$, whereas they have similar mobility in HCL_LEV_1_2. Perkins et al.[99] justified the self-diffusion data of $[Cl]^-$ and HBD in reline indicating that in spite of the strong hydrogen bonding between both compounds their movements are not tied. On the contrary in the case of CHCL_LEV_1_2 mobility of $[Cl]^-$ and HBD (LEV) seems to be strongly correlated.

A key point in the determination of self-diffusion coefficients from molecular dynamics simulations is if the condition of fully diffusive regime is reached in the timeframe used, which is commonly measured through the so-called βparameter, defined as the slope of log-log plots of msd vs. simulation time.

Fully diffusive regime is reached when β=1 whereas subdiffusive regimes are characterized by β<1. Perkins et al.[99] showed that in the case of reline at 298 K fully diffusive regime is reached at 30 ns, whereas it is reached at 10 ns for CHCL_LEV_1_2 in this work. This may be justified considering that reline viscosity[94] is twice that for CHCl_LEV_1_2, which leads to larger molecular mobilities (as showed by the larger self-diffusion coefficients) and thus to diffusive regimes reached at shorter simulation times. Dynamic viscosity was calculated using Green-Kubo method leading to 265 mPa×s at 298 K, which is in fair agreement with 226.8 mPa×s obtained by Florindo et al.[60]

Vaporization enthalpy may be obtained from molecular dynamics simulations as the internal energy difference between liquid and gas phases (plus and $R \times T$ term), which can be assimilated to the difference between potential energies.[100,101] The gas phase was modeled considering a low density cage (0.006 g×cm^{-3}) composed by a $[CH]^+$ - $[Cl]^-$ ion pair and two LEV molecules not interacting with [CH][Cl]. In the course of gas phase simulations (10 ns long), LEV molecules aggregated with [CH][Cl] ion pair. The main contributions to CHCL_LEV_1_2 vaporization enthalpy at 298 K are summarized in Table 1 showing that the main contribution to the potential energy differences between liquid and gas phases is non-bonded term rising from intermolecular interactions, whereas bonded and intra-molecular non-bonded terms are almost negligible. Likewise, the vaporization enthalpy CHCL_LEV_1_2 is lower than those values reported in the literature for ionic liquids,[100] which is in agreement with the strong effect of strong coulombic effects rising in ionic liquids whereas the strength of LEV – ions intermolecular interactions in the studied DES are weaker. This effect should be confirmed experimentally in future works.

The structure of CHCL_LEV_1_2 is strongly dominated by the strength and nature of intermolecular interactions, E_{inter}, and thus, intermolecular interaction energies were quantified and reported in Figure 10. Anion – cation are the stronger intermolecular interactions as it may be expected considering their ionic nature. Regarding the ion-[LEV] interactions, it should be remarked the positive E_{inter} values for $[Cl]^-$ - [LEV], rising from the positive coulombic contribution because both molecules are negatively charged (see Methods section), in contrast with the larger and negative E_{inter} values (85 % coulombic contribution) for $[CH]^+$ – [LEV], both moderately decreasing temperature. Nevertheless, the large total E_{inter} shows the development of very effective intermolecular interactions in the studied DES, which remains with minor changes in the studied temperature range. These results are in contrast with those obtained for reline by Sun et al.[102] which showed that $[Cl]^-$ - HBD interactions are roughly three times larger than $[CH]^+$ – HBD in the case of urea.

The main structural features for CHCL_LEV_1_2 may be obtained from the radial distribution functions, $g(r)$, reported in Figure 11. Results in Figure 11a show ion-ion interaction in CHCL_LEV_1_2. The anion-cation strong interaction developing the ion pair is well defined by the strong and narrow peak at short distance in Figure 11a, whereas very minor features appear for this interaction at larger distances. Anion-anion interaction is characterized by a broad peak followed by a shoulder in the 5 to 10 Å range, which is in contrast with the cation-cation interactions, which are characterized by a strong intermolecular hydrogen bonding inferred from the narrow first peak in Figure 11a followed by three weaker and wider peaks, which show that $[CH]^+$ develop well-defined hydrogen bonding through the cation hydroxyl group. For the analysis of ion-[LEV] interactions, it should be remarked that LEV has three sites that may act as donors and / or acceptors for developing hydrogen bonding: *i*) the oxygen atom in -C=O for –COO group, Ol1, *ii*) the –OH in –COO group, Ol2 and Hl, and *iii*) the oxygen atom in –CO terminal group, Ol3, Figure 11. Radial distribution functions for these three groups are reported in Figure 11b with regard to ion-LEV interactions. Results in Figure 11b show the development of hydrogen bonding with LEV both for the anion and cation, the $[Cl]^-$ - LEV interaction (developed through the Hl site) lead to stronger peaks than $[CH]^+$ - [LEV] but the $[Cl]^-$ - [LEV] peak appear at 0.3 Å larger distance, and thus this interaction should be weaker than $[CH]^+$ - LEV. The $[CH]^+$ - LEV interactions are characterized by the development of hydrogen bonding between the $[CH]^+$ hydroxyl hydrogen, Hc, and two possible acceptor sites in [LEV] (Ol1, and Ol3), which are characterized by well defined narrow peaks appearing at roughly 1.8 Å but being larger for the interaction through Ol1 site. The interaction through Ol2 has shown poor interactions according to wide peak in Figure 11b. Likewise, results in Figure 11b show the development of $[CH]^+$ - [LEV] hydrogen bonding in which [LEV] acts as a hydrogen bond donor, Hl, and $[CH]^+$ as acceptor, Oc, although being weaker than those in which [LEV] act as hydrogen bond acceptor.

Therefore, the $[CH]^+$ - [LEV] interaction is mainly developed through the Ol1 site with weaker interactions through Ol3 site and through Hl-Oc interaction. [LEV]-[LEV] interaction is analyzed in Figure 11c showing that the main interaction is developed between the Hl and Ol1 sites, with weaker contributions through the hydrogen bonding through the Ol3 position and almost negligible interactions through the Ol2 site. Therefore, the [LEV] hydroxyl group acts as a strong hydrogen bond donor, both with $[CH]^+$ and other [LEV] molecules and the intermolecular hydrogen bonding are developed mainly through Ol1, and in minor extension, Ol3 acceptor sites.

A most detailed picture of the molecular arrangement in CHCL_LEV_1_2 can be obtained from spatial distribution functions, SDF, reported in Figure 12. The $[CH]^+$-$[CH]^+$ interaction is well defined in Figure 12a showing the high density cap above the oxygen atom in the hydroxyl group (accepting H-bonds) and below the hydrogen atom in hydroxyl group (donor for H-bonds), together with a big cap surrounding the remaining $[CH]^+$ molecular regions showing the prevailing role of the hydroxyl group for the development of intermolecular hydrogen bonds. Cl^- anions develop a high-density region in the vicinity of the Hc group, Figure 12b, in agreement with the strong peak in Figure 11a. The arrangement of LEV Hl atoms around $[CH]^+$, Figure 12c, follows a similar pattern to that of Hc, Figure 12a, showing that [LEV] and $[CH]^+$ molecules occupy the same regions around a central $[CH]^+$ ion. Regarding the structuring around [LEV], the high density cap above the Ol1 atom of Hc atoms, Figure 12d, show that $[CH]^+$ cations tend to concentrate above the Ol1 in LEV – COOH group, with weaker interactions through the remaining [LEV] H-bond acceptor sites. The $[Cl]^-$ - [LEV] interactions is mainly developed through the hydroxyl head group in [LEV], Figure 12d, but being placed at larger distances than in the case of Cl^- around $[CH]^+$. Finally, LEV – LEV interactions lead to high-density regions above the Ol1 group, Figure 12e.

The structural features inferred from Figure 11 and Figure 12 show the development of H-bonding between all the involved molecules through the $[CH]^+$ hydroxyl site and LEV – COOH group, and thus, the number of H-bonds is reported in Figure 13. A large number of H-bonds is developed with the $[Cl]^-$ anion both through the Hc ($[CH]^+$) and Hl (LEV) sites, being larger for [LEV]-$[Cl]^-$. The number of $[CH]^+$ - $[CH]^+$ H-bonds (Hc – Oc) is lower than that for $[CH]^+$ - [LEV] (Hc-Ol1, Hc-Ol2 and Hc-Ol3), which are larger for Hc-Ol1 site as expected from results in **Error! Reference source not found.**b, in agreement with results in Figure 12a and Figure 12d. [LEV]-[LEV] H-bonds are developed mainly through the Ol1 site with minor interactions through the Ol3 site and discarding the H-bonding through Ol2 site. These results should be analyzed considering that two LEV molecules interact with a central $[Cl]^-$ anion, and thus, this lead to larger LEV-LEV and $[CH]^+$ - LEV H-bonding.

The development of strong H-bonding between all the involved molecules in CHCL_LEV_1_2 requires an additional analysis about the lifetimes of these intermolecular interactions. This analysis was carried out through the calculation of residence time, t_{res}, of relevant sites around others for characterizing H-bonding. Residence time was calculated from the exponential decay of conditional probability for a site to stay within a sphere of defined radius around another molecular site, as explained in previous work.[103] Sun et al.[102] reported lifetimes of hydrogen bonds in reline DES, showing lifetimes lower than 13 ps for all the reported H-bonds in the eutectic composition, with values of 12.574 ps for the $[CH]^+$ - Cl^- H-bond, 2.397 ps for the urea (HBD) – $[Cl]^-$ H-bond, and 2.952 ps for the urea – urea interaction. These values are lower than those reported for CHCL_LEV_1_2 in Figure 14a, but it may be justified that the distance criteria used to define residence times in Figure 14a (6.0 Å) is roughly the double to that used Sun et al.[102] to define their H-bonds lifetimes (roughly 3 Å). The criteria used in Figure 14 consider the existence of a second solvation shell around each hydrogen bond donor site, and thus, although H-bonds are destroyed for distances larger than 3.0 Å, those atoms staying in the 3 to 6 Å rise from the reorganization of the local H-bonding structure and they may develop a new H-bond in a fast way, and thus using 6.0 Å may give a realistic picture of the H-bonding around a certain site. The residence times reported in Figure 14a are very similar for all the considered interactions being in the 35 to 55 ps range. Moreover, the analysis of the temperature evolution of residence times follow a similar non-Arrhenius pattern for all the studied interactions, and thus, confirming a strong correlation between the dynamics of all the studied H-bonds.

Results in Figure 15 show the changes in intermolecular interaction energy upon CO_2 absorption for CO_2 pressures up to 10 bar. The structure of CHCL_LEV_1_2 does not change upon CO_2 absorption from the energetic viewpoint, ion-ion, ion-LEV and LEV-LEV E_{inter} suffer very minor changes with increasing CO_2 mole fraction, **Error! Reference source not found.**a; e.g. for $[CH]^+$ - $[Cl]^-$, E_{inter} decreases just a 2.5 % in absolute value. Therefore the liquid structure of CHCL_LEV_1_2 is able to accommodate CO_2 molecules without remarkable changes in its mechanism of intermolecular interaction. Regarding to the strength of interactions between CO_2 and molecules present in CHCL_LEV_1_2, results in Figure 15b show that the strength of interactions follow the ordering [LEV] > $[CH]^+$> $[Cl]^-$, and thus, pointing to a preferential absorption of CO_2 molecules through LEV molecules. The structural features of CO_2 absorption are summarized in Figure 16 for radial distribution functions. The arrangement of CO_2 molecules around $[CH]^+$, Figure 16a, show that CO_2 molecules are placed both around the cation hydroxyl group and also around the methyl groups, following a similar patterns for the first solvation sphere although for the hydroxyl group two additional maxima in *g(r)* points to a slightly stronger interaction through that site. This is confirmed by spatial distribution functions in Figure 17a, which although show high density caps around the

$[CH]^+$ hydroxyl group also shows a very symmetrical distribution of CO_2 molecules around the methyl group, which would justify the sharp and narrow peak around the $[CH]^+$ nitrogen atom in $g(r)$ reported in Figure 17a. The CO_2 molecules are also strongly structured around $[Cl]^-$, Figure 17b, the sharp peak in $g(r)$ follows a similar pattern to the interaction between CO_2 molecules and Hc site in $[CH]^+$, and thus, as the absorption of CO_2 molecules does not disrupt anion-cation interactions, CO_2 may interact efficiently with both ions at the same time. The CO_2-[LEV] interaction is characterized by the strong features in $g(r)$ around the Hl and Ol3 sites, with weaker interactions through the Ol3 site, which lead to a CO_2 distribution around the terminal [LEV] methyl group. Therefore, CO_2 molecules are placed around the LEV hydroxyl group and also around the terminal groups of [LEV] molecule, Figure 17b, with minor concentration around the Ol1 group.

Upon increasing CO_2 absorbed amounts, these molecules tend to clusterize, for 1 bar CO_2 pressure, the number of absorbed molecules is very low, and thus, CO_2 clusters were not observed, Figure 18, but with increasing CO_2 mole fraction (increasing pressure) a well defined peak at 4.3 Å in $g(r)$ is obtained followed by a second and wider peak. The position of these peaks does not change with increasing pressure, only their intensity increases with increasing CO_2 absorbed amount. The corresponding running integrals for these $g(r)$ shows that the first solvation sphere, integrating up to the first minimum, around a central CO_2 molecule contains at least two additional CO_2 molecules, whereas another two additional CO_2 molecules may be found in the second solvation sphere, for the highest studied pressures.

The dynamic of CO_2 absorbed molecules may be analyzed considering the residence times of CO_2 around both ions and [LEV] molecules, Figure 19. Results show that the mobility of CO_2 molecules is almost twice around $[Cl]^-$ and [LEV] than around $[CH]^+$, and in all the cases these mobility increases with increasing CO_2 pressure, with the exception of the change from 1 to 4 bar. This result is surprising considering the strength of the interactions between CO_2 molecules and CHCL_LEV_1_2 molecules reported in Figure 15b, which led to larger E_{inter} for CO_2 – LEV than for the other interaction pairs, but it may be explained considering steric factors around the $[CH]^+$ which hinder the molecular mobility of CO_2 molecules interacting with this ion in comparison with the CO_2 absorption sites around LEV.

A remarkable feature that should be analyzed to understand the mechanism of absorption of CO_2 molecules in CHCL_LEV_1_2 is the interfacial behavior of CHCL_LEV_1_2 – CO_2 systems. The CO_2 capturing from flue gases requires that CO_2 molecules are adsorbed in the sorbent – gas interface and then they diffuse from the interfacial region toward the bulk DES. Therefore, to analyze this fact a simulation on the properties of CO_2-DES interface was carried out using molecular dynamics in this work. Pure CO_2 gas was put in contact with CHCL_LEV_1_2 and the behavior was followed as a function of time. For comparison purposes the CHCL_LEV_1_2 – vacuum interface was also simulated. Density profiles in Figure 20a,b,c allow to characterize the molecular arrangements of ions and LEV molecules in the interfacial region with vacuum. The density profiles for ions and LEV center-of-mass in Figure 20a show that [LEV] molecules occupy outer regions close to the vacuum layer with ions being placed in inner regions, therefore, the CHCL_LEV_1_2 – vacuum interface is composed mainly of [LEV] molecules, Figure 21a. Figure 20b shows that $[CH]^+$ cations tend to orientate parallel to the interface, whereas results in Figure 20c show how [LEV] molecules are placed perpendicular to the vacuum interface with –COOH group pointing toward the bulk fluid and terminal methyl group exposed to the vacuum layer. These molecular arrangements do not change significantly when CHCL_LEV_1_2 is put in contact with a CO_2 gas layer, very subtle structural changes occur to accommodate adsorbed CO_2 molecules in the interface, Figure 20d,e,f, but ions and LEV arrangement is similar to the vacuum interface, Figure 21b.

The main structural feature of CHCL_LEV_1_2 – CO_2 interface is the formation of a strongly adsorbed layer of gas molecules, Figure 21b, which is formed in the first stages of simulations (0 to 1 ns), then upon the formation of this initial layer its size increases upon increasing simulation time, Figure 22. The main characteristic of this adsorbed layer is that CO_2 molecules are adsorbed very quickly but once they are in this layer above CHCL_LEV_1_2, in contact mainly with [LEV] molecules, their mobility is very reduced, and thus, the time that CO_2 molecules remains in this layer on top of CHCL_LEV_1_2 is long, Figure 22. In the first 6 ns of simulation, all the CO_2 molecules were placed in the adsorbed layer whereas no CO_2 molecules were able to diffuse toward the bulk CHCL_LEV_1_2. The layer of CO_2 adsorbed molecules develop strong interactions with [LEV] molecules and weaker ones with $[CH]^+$, especially when the adsorbed layer is wide enough (simulation times > 4 ns, Figure 23), which is in agreement with the interface structure inferred from Figure 20a. This persistence of the CO_2 molecules in the initially adsorbed layer at the CHCL_LEV_1_2 - gas interface before moving toward the bulk liquid phase should be considered for any industrial application of this DES as a carbon capture agent, the kinetics of the CO_2 absorption process (largely controlled by the high affinity of CO_2 molecules for the [LEV]-rich interfacial region) has to be analyzed together with thermodynamics factors controlling capturing process.

3.8 Short-Range Properties through DFT

Previously, CHCL_LEV_1_2 structural features and CO_2 capture mechanism have been analyzed in the context of MD simulations. In this section, the main features regarding to CHCL_LEV_1_2 and CHCL_LEV_1_2$\cdots CO_2$ systems are assessed trough DFT simulations. The bulk effects that are studied though DFT simulations allow detailed insights of the studied systems at molecular level as that is useful forecasting macroscopic behavior. Figures 24, 25 and 26 plot optimized structures for [CH][Cl], CHCL_LEV_1_2 and CHCL_LEV_1_2$\cdots CO_2$ systems, respectively. Table 2 gathers distances for those intermolecular interactions found in the context of AIM theory, along the electronic density value (ρ) for the corresponding BCP. Prior to analyze CHCL_LEV_1_2 and CHCL_LEV_1_2$\cdots CO_2$ systems, this paragraph shows the main features for the [CH][Cl] ionic compound (Figure 24). As expected, the main interaction between both ions is due to a coulombic attraction between both ions, which agrees with the high binding energy for the ionic pair interaction, $|\Delta E_{IP}|$ = 511.81kJ×mol^{-1}. For the ionic pair, the intermolecular charge transfer (CT_{IP}) is equal to 0.161e$^-$. In addition, chloride atom stabilizes four intermolecular hydrogen bonds with the cation (d_1-d_4), wherein the strongest one is carried out through the OH (cation) group.

In accordance with MD simulations, the optimized structure for CHCL_LEV_1_2 (Figure 15) is mainly characterized by intermolecular hydrogen bonds between the chloride atom and both levulinic acid molecules. Both levulinic acid molecules (through H atom of COOH group) yield an H-bond with the chloride atom (d_5 and d_6 for LEV1 and LEV2, respectively). In addition, both molecules also establish several H-bonds with choline cation. All these bonds (d_7, d_8 and d_9, d_{10} for LEV1 and LEV2, respectively) are carried out through COOH group (levulinic acid) and methylic hydrogen atoms (choline), except $d_{7,}$ which is formed between COOH group and -CH_2 group adjacent to OH motif. As can be seen in Table 2, Cl^- - LEV interactions yields the largest electronic density values, i.e., the key interactions in the DES structure are those carried out between the levulinic molecules and the chloride atoms. The interaction energy between ionic pair and [LEV] molecules was $|\Delta E_{DES}|$ = 141.93 kJ×mol^{-1} (Figure 25), showing energetically favored DES. Figure 25 also collect computed charges over cation, anion and levulinic acid motifs. The largest change on the charges is noted for chloride atom, which decreases its charge 0.155e$^-$ (regarding [CH][Cl] ionic pair. For CHCL_LEV_1_2 some negative charge is transferred from the anion up to levulinic acid molecules, 0.066e$^-$ and 0.074e$^-$ for LEV1 and LEV2, respectively. In addition, there are also some hydrogen bonds between both ions, very similar to those ones reported in Figure 24. In this sense, chloride atom yields three hydrogen bonds (d_1-d_3) with the cation, which are weakened compared with the ionic compound. Thus, d_1 suffers an elongation of 0.157 Ǻ, while its electronic density value diminishes 0.0108 a.u. From CHCL_LEV_1_2 optimized structure, binding energy for the ionic pair has been also calculated through a single point calculation, which is also used for estimating the interaction strength. For CHCL_LEV_1_2, $|\Delta E_{IP}|$ = 503.87kJ×mol^{-1}, i.e., DES formation brings out a weaning on the ionic pair interaction of around 7.93 kJ×mol^{-1}.

Figure 26 draws optimized structure for CHCL_LEV_1_2···CO_2. Three different arrangements (*a*, *b*, and *c*) were found for the interaction between the DES and the CO_2 molecule. As noted from MD simulations, the structure of CHCL_LEV_1_2 does not change upon CO_2 absorption. In this sense, the same intermolecular H-bonds reported for the DES structure (d_1-d_{10}) were also found in presence of CO_2 molecule. As can be seen in Table 2, intermolecular distances and their electronic density values slightly change in presence of CO_2 molecule. ΔE_{IP} y ΔE_{DES} were also computed for CHCL_LEV_1_2···CO_2 optimized structures. For these arrangements, $|\Delta E_{IP}| \simeq 503.30$ kJ×mol^{-1} and $|\Delta E_{DES}| \simeq 139.80$ kJ×mol^{-1}, very similar than those values computed for CHCL_LEV_1_2. There are some similarities between arrangements *a* and *c*. From a structural viewpoint, for arrangement a/c, CO_2 molecule is mainly linked to Cl atom (d_{11}/d_{14}) and COOH group of LEV1/LEV2 (d_{12}/d_{15}), being the latter this one with the largest electronic density values for the associated BCP. In addition, d_{11}/d_{12} features are similar to d_{14}/d_{15}. Nevertheless, $|\Delta E_{DES\text{-}CO2}{}^{a}|$ (17.46 kJ×mol^{-1}) is larger than $|\Delta E_{DES\text{-}CO2}{}^{b}|$ (14.77 kJ×mol^{-1}). This energy difference could be related with difference charge distributions. For arrangement *a*, LEV1 is more negative than LEV1 in CHCL_LEV_1_2, which allows a slightly large charge transfer up to the CO_2 molecule (whose charge is 0.027e$^-$). However, negative charge over LEV2 in arrangement *c* does not vary, being the charge transfer up to CO_2 molecule of around 0.014 e$^-$. As far as Cl charge are concerned, the largest charges are noted for arrangement *c*. Regarding to arrangement *b*, CO_2 molecules are mainly interacting with COOH group of LEV2, through d13 which is stronger (based on lower /larger intermolecular distances /electronic density values) than those interactions found in arrangements *a* and *c*. Although the charge over LEV2 is still very small, LEV2 decreases its charge 0.037 e$^-$, while charges over LEV1, choline and chloride remain unaffected. This interactions provides the largest binding energies for CO_2 capture, $|\Delta E_{DES\text{-}CO2}{}^{c}|$ = 24.90 kJ×mol^{-1}. According with DFT results, CHCL_LEV_1_2 displays three different positions for CO_2 adsorption, whose high values would point out energetically favored process.

4. Conclusions

This extensive study combines both experimental and theoretical investigation of the DES system made by mixing CHCl and LEV with 1:2 mixing ratio. Experimental studies are focused on obtaining detailed physical characteristics of the studied system; and CO_2 solubility at high pressures was the most important part of the experimental study. A promising 2.316 mmol of CO_2 per gram of DES sample at 293 K has been obtained at 50 bars. Moreover, a detailed corrosivity study that deals with CO_2 saturated DES system showed a great corrosion resistance with a corrosion rate of 0.027 mm/year, whereas the same experiments showed 0.54 mm/year corrosion rate for CO_2 saturated MEA system.

Molecular dynamics and DFT results allowed analyzing the structural properties of CHCL_LEV_1_2 both in pure state and after CO_2 absorption. CHCL_LEV_1_2 liquid phase is characterized by the development of intermolecular hydrogen bonding between [LEV molecules and both Cl^- and $[CH]^+$ ions, with [LEV] molecules mainly accepting H-bonds through the Ol1 atom in -COOH group and as a H-bond donor through the hydrogen atom of the hydroxyl group. Likewise, $[CH]^+$ are also self associated through H-bonding, and thus, the characteristics of the functional groups available in the molecules composing CHCL_LEV_1_2 allow the development of a very efficient network of H-bonds, which is the main reason of the properties of this fluid. This structuring does not change upon CO_2 absorption for pressures lower than 10 bars, with the CO_2 molecules developing stronger interactions with [LEV] molecules than with the ions. The CO_2 capturing process by CHCL_LEV_1_2 is also characterized by the strong affinity of CO_2 molecules for the interfacial DES - gas region, which is very rich in [LEV] molecules, and thus, leading to large lifetimes of adsorbed molecules in the interfacial region with slow migration toward the bulk fluid region.

The combined experimental and computational results reported in this work allow a detailed characterization of CHCL_LEV_1_2 DES both from the macroscopic and nanoscopic viewpoints and its relationship with their possible use as carbon capture agent.

Acknowledgements

This work was made possible by NPRP grant # 6-330-2-140 from the Qatar National Research Fund (a member of Qatar Foundation), Ministerio de Economía y Competitividad (Spain, project CTQ2013-40476-R) and Junta de Castilla y León (Spain, project BU324U14). Gregorio García acknowledges the funding by Junta de Castilla y León, cofunded by

European Social Fund, for a postdoctoral contract. We also acknowledge The Foundation of Supercomputing Center of Castile and León(FCSCL, Spain),Computing and Advanced Technologies Foundation of Extremadura (CénitS, LUSITANIA Supercomputer, Spain), and Consortium of Scientific and Academic Services of Cataluña (CSUC, Spain) for providing supercomputing facilities. The statements made herein are solely the responsibility of the authors.

Associated content

Electronic Supplementary Information (ESI)

Table S1 (forcefield parameterization), Table S3 (physicochemical properties), Table S4 (NMR data) and Figure S1 (in-situ FTIR apparatus setup), Figure S2 (sorption apparatus setup) and Figure S3 (in-situ FTIR data).

Table 1. Energy differences between liquid and gas phases for CHCl_LEV_1_2 calculated from molecular dynamics simulations. ΔH_{vap} stands for vaporization enthalpy, $\Delta E_{pot,BONDED}$ for bonded potential energy (bond, angle and dihedral contributions) difference, $\Delta E_{pot,NON\text{-}BONDED}$ for the non-bonded potential energy (Lennard-Jones and coulombic contributions) difference, $\Delta E_{pot,TOT}$ for the total potential energy difference and $\Delta E_{pot,INTER}$ for the intermolecular interactions potential energy difference. All values at 298 K

ΔH_{vap} / kJ×mol^{-1}	$\Delta E_{pot,TOT}$ / kJ×mol^{-1}	$\Delta E_{pot,BONDED}$ / kJ×mol^{-1}	$\Delta E_{pot,NON\text{-}BONDED}$ / kJ×mol^{-1}	$\Delta E_{pot,INTER}$ / kJ×mol^{-1}
52.05	49.57	-4.76	54.34	40.74

Table 2. Intermolecular distances along their corresponding electronic density (ρ) values for the main intermolecular interactions for [CH][Cl], CHCL_LEV_1_2 and CHCL_LEV_1_2···CO_2 systems estimated at DFT/B3LYP-D2/6-31+G** theoretical level. See Figures 17, 18 and 19. Estimated binding energies are also collected.

		Length/ Å	ρ / a.u.		Length/ Å	ρ / a.u.	ΔE / kJ×mol^{-1}
[CH][Cl]	d_1	2.084	0.0341	d_3	2.418	0.0184	$\lvert\Delta E_{IP}\rvert$=511.81
	d_2	2.383	0.0197	d_4	2.809	0.0104	
CHCL_LEV_1_2	d_1	2.241	0.0233	d_7	2.317	0.0132	$\lvert\Delta E_{DES}\rvert$=141.93
	d_2	2.626	0.0120	d_8	2.528	0.0099	$\lvert\Delta E_{IP}\rvert$=503.83
	d_3	2.637	0.0116	d_9	2.366	0.0113	
	d_5	2.069	0.0331	d_{10}	2.375	0.0117	
	d_6	2.088	0.0315				
CHCL_LEV_1_2···CO_2 a)	d_1	2.247	0.0230	d_8	2.526	0.0100	$\lvert\Delta E_{DES\text{-}CO2}{}^{a}\rvert$=17.46
	d_2	2.646	0.0115	d_9	2.381	0.0112	$\lvert\Delta E_{DES}{}^{a}\rvert$=140.18
	d_3	2.661	0.0110	d_{10}	2.377	0.0114	$\lvert\Delta E_{IP}{}^{a}\rvert$=503.03
	d_5	2.076	0.0329	d_{11}	3.468	0.0050	
	d_6	2.098	0.0307	d_{12}	2.960	0.0082	
	d_7	2.351	0.0122				
CHCL_LEV_1_2···CO_2 b)	d_1	2.241	0.0232	d_7	2.325	0.0130	$\lvert\Delta E_{DES\text{-}CO2}{}^{b}\rvert$=5.93
	d_2	2.666	0.0112	d_8	2.511	0.0101	$\lvert\Delta E_{DES}{}^{b}\rvert$=140.12
	d_3	2.632	0.0117	d_9	2.471	0.0094	$\lvert\Delta E_{IP}{}^{b}\rvert$=503.39
	d_5	2.073	0.0329	d_{10}	2.383	0.0113	
	d_6	2.066	0.0332	d_{13}	2.733	0.0128	
CHCL_LEV_1_2···CO_2 c)	d_1	2.246	0.0230	d_8	2.503	0.0102	$\lvert\Delta E_{DES\text{-}CO2}{}^{c}\rvert$=3.52
	d_2	2.628	0.0120	d_9	2.363	0.0115	$\lvert\Delta E_{DES}{}^{c}\rvert$=139.10
	d_3	2.630	0.0118	d_{10}	2.360	0.0120	$\lvert\Delta E_{IP}{}^{c}\rvert$=503.51
	d_5	2.080	0.0322	d_{14}	3.446	0.0051	
	d_6	2.092	0.0317	d_{15}	2.949	0.0078	
	d_7	2.311	0.0133				

Figure Captions.

Figure 1. Molecular structure of [CH][Cl] salt and levulinic acid.

Figure 2. Experimental set-up for electrochemical corrosion tests

Figure 3. Experimental (a) density, ρ, refraction index, n_D, and (b) viscosity, η, data for CHCL_LEV_1_2 DES system. In panel b, a comparison of η data with those reported by Florindo et al.[60] is reported considering the water content (wt %) of used samples. Error bars are not reported because they are smaller than point size.

Figure 4. FTIR characterization results for [CH][Cl], [LEV] and CHCL_LEV_1_2 DES system.

Figure 5. Thermal gravimetric analysis of CHCL_LEV_1_2 DES system.

Figure 6. Corrosion resistance performance experiments for CO_2 saturated CHCL_LEV_1_2 DES system and its comparison with CO_2saturated MEA system.

Figure 7. High pressure CO_2 solubility in CHCL_LEV_1_2 DES system at various isotherms up to 30 bars. Points show experimental data and lines are plotted for guiding purposes.

Figure 8. Isobaric CO_2 solubility in CHCL_LEV_1_2 DES kinetics: (a)1 bar and (b) 30 bars. Points show experimental data and lines are plotted for guiding purposes.

Figure 9. Deviation between density data for CHCL_LEV_1_2 calculated from molecular dynamics simulations, ρ_{MD}, and experimental density, ρ_{EXP}, for experimental data obtained in this work and for data by Florindo et al. ρ_{MD} at 1 bar and ρ_{EXP} at atmospheric pressure.

Figure 10. Intermolecular interaction energies, E_{inter}, in CHCL_LEV_1_2 calculated from molecular dynamics simulations at different temperatures and 1 bar. C stands for $[CH]^+$, A for Cl^-, LEV for levulinic acid, and TOTAL for the sum of all intermolecular interaction contributions. Lines show linear fits.

Figure 11. Site – sire radial distribution functions, $g(r)$, in CHCL_LEV_1_2 calculated from molecular dynamics simulations at 298 K and 1 bar.

Figure 12. Spatial distribution functions of relevant atoms around [CH] cation (panels a,b and c) and around LEV (panels d, e and f) in CHCL_LEV_1_2 calculated from molecular dynamics simulations at 298 K and 1 bar. All values show isodensity plots corresponding to 4-times bulk density. Atom names as in Figure 14.

Figure 13. Number of hydrogen bonds, N_H, between the different donor-acceptor interaction sites for CHCL_LEV_1_2 calculated from molecular dynamics simulations. Values calculated for a simulation box containing 250 [CH][Cl] ion pairs and 250 LEV molecules. Reported values show averages in the 298 K to 348 K temperature range with error bars showing standard deviations for that temperature range. All values calculated considering 3.0 Å and 50.0º as donor-acceptor distance and angle cut-offs, respectively.

Figure 14. Residence time, t_{res}, of selected atoms around other atoms in DES_LEV_1_2. t_{res} was calculated from the exponential decay of conditional probability P with R = 6.0 Å.

Figure 15. Intermolecular interaction energies, E_{inter}, in CHCL_LEV_1_2 + CO_2 systems calculated from molecular dynamics simulations at different CO_2 pressures and 298 K. C stands for $[CH]^+$, A for Cl^-, LEV for levulinic acid. Lines are plotted for guiding purposes.

Figure 16. Site – sire radial distribution functions, $g(r)$, in CHCL_LEV_1_2 + CO_2 systems calculated from molecular dynamics simulations at 10 bar CO_2 pressure and 298 K. Atom names as in Figure 14; CD stands for carbon atoms in CO_2, Hm stands for all the hydrogen atoms in methyl groups bonded to Nc atom in $[CH]^+$; Ht stands for all the hydrogen atoms in methyl group of LEV.

Figure 17. Spatial distribution functions of CO_2 carbon atoms around (a) $[CH]^+$ and (b) LEV, in CHCL_LEV_1_2 + CO_2 systems calculated from molecular dynamics simulations at 10 bar CO_2 pressure and 298 K. All values show isodensity plots corresponding to 4-times bulk density.

Figure 18. CD – CD site – site radial distribution functions, $g(r)$, in CHCL_LEV_1_2 + CO_2 systems calculated from molecular dynamics simulations as a function of CO_2 pressure and 298 K. CD stands for carbon atoms in CO_2.

Figure 19. Residence time, t_{res}, of CO_2 carbon atoms around the center of mass of $[CH]^+$, $[Cl]^-$,and LEV molecules in CHCL_LEV_1_2 + CO_2 systems calculated from molecular dynamics simulations as a function of CO_2 pressure, p, and 298 K. CD stands for carbon atoms in CO_2. t_{res} was calculated from the exponential decay of conditional probability P with R = 6.0 Å.

Figure 20. Density profiles for (a,d) center of mass of $[CH]^+$, Cl^- and LEV, and for relevant atoms in (b,e) $[CH]^+$ and (c,f) LEV, molecules in CHCL_LEV_1_2 + (a,b,c) vacuum and (d,e,f) CO_2 interfaces systems calculated from molecular dynamics simulations at 298 K. z stands for the coordinate perpendicular to the corresponding interfaces, and z_{GDS} for the coordinate of the Gibbs dividing surface. Profiles obtained as averages in the 4 to 5.5 ns timeframe.

Figure 21. Snapshot of the CHCL_LEV_1_2 – (a) vacuum or (b) CO_2 interfaces calculated from molecular dynamics simulations at 298 K. Color code: (blue) $[CH]^+$, (green) Cl^-, (red) LEV, and (yellow) CO_2. Snaphots obtained after 5.5 ns simulations.

Figure 22. Density profiles for CO_2 molecules in CHCL_LEV_1_2 + CO_2 interfacesystem calculated from molecular dynamics simulations at 298 K. z stands for the coordinate perpendicular to the corresponding interfaces, and z_{GDS} for the coordinate of the Gibbs dividing surface. Profiles obtained as averages in the reported timeframes.

Figure 23. Intermolecular interaction energy, E_{int}, between CO_2 and molecules forming CHCL_LEV_1_2 CHCL_LEV_1_2 + CO_2 interfacesystem as a function of simulation time, calculated from molecular dynamics simulations at 298 K.

Figure 24. Optimized structures for [CH][Cl] at B3LYP-D2/6-31+G** level, along the main structural parameters related with intermolecular interactions. Computed charges over choline (q^{CH+}) and chloride (q^{Cl-}) motifs, as well as the binding energy (ΔE_{IP}) for ionic pair interaction are also shown**.**

Figure 25. Optimized structures for CHCL_LEV_1_2 at B3LYP-D2/6-31+G** level, along the main structural parameters related with intermolecular interactions. Computed charges over choline (q^{CH+}), chloride (q^{Cl-}) and levulinic (q^{Lev}) motifs, as well as the binding energy (ΔE_{DES}) for corresponding for DES formation are also shown**.**

Figure 26. Optimized structures for CHCL_LEV_1_2$\cdots CO_2$ system (three different arrangements were found) at B3LYP-D2/6-31+G** level, along the main structural parameters related with intermolecular interactions. Computed charges over choline (q^{CH+}), chloride (q^{Cl-}), levulinic (q^{Lev}) and CO_2 (q^{CO2}) motifs, as well as the binding energy ($\Delta E_{DES\text{-}CO2}$) corresponding for CO_2 catch by selected DES are also shown. For clarity, intermolecular bonds labels corresponding to DES have been omitted, since we followed the same nomenclature used in Figure 25.

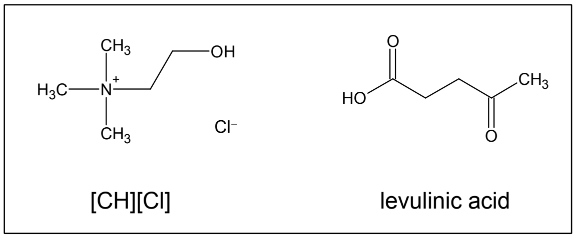

Figure 1.

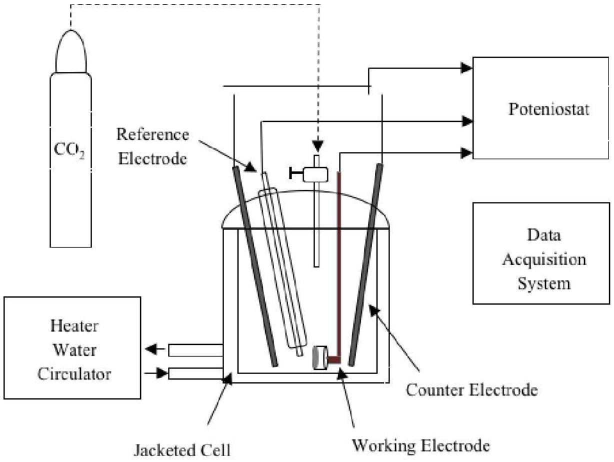
CO$_2$
Reference Electrode
Poteniostat
Data Acquisition System
Heater Water Circulator
Counter Electrode
Jacketed Cell
Working Electrode

Figure 2.

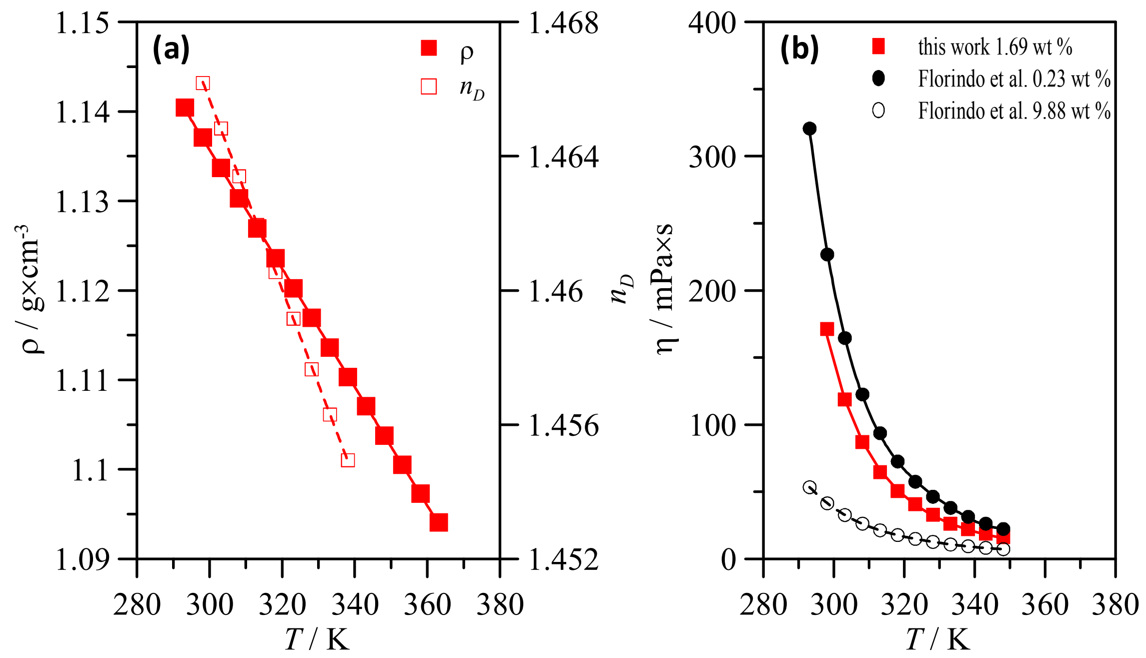
(a)
ρ
n_D
ρ / g×cm-3
n_D
1.15
1.14
1.13
1.12
1.11
1.1
1.09
1.468
1.464
1.46
1.456
1.452
280
300
320
340
360
380
T / K
(b)
this work 1.69 wt %
Florindo et al. 0.23 wt %
Florindo et al. 9.88 wt %
η / mPa×s
400
300
200
100
0
280
300
320
340
360
380
T / K

Figure 3.

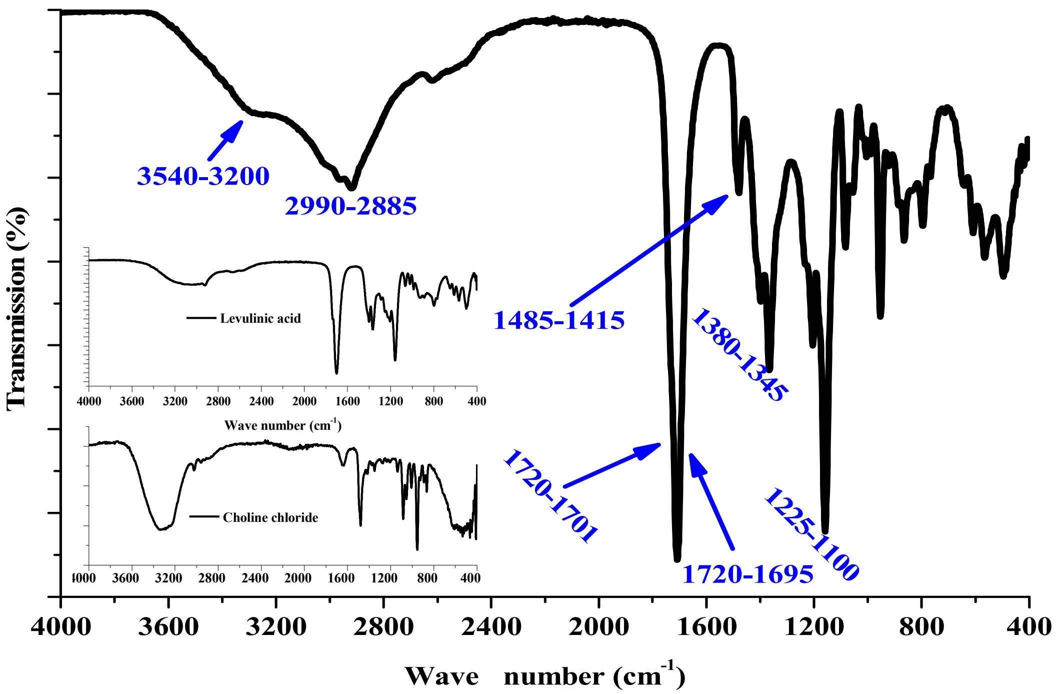
Transmission (%)
3540-3200
2990-2885
1485-1415
1380-1345
1720-1701
1720-1695
1225-1100
Levulinic acid
Wave number (cm^{-1})
Choline chloride
4000
3600
3200
2800
2400
2000
1600
1200
800
400
Wave number (cm^{-1})

Figure 4.

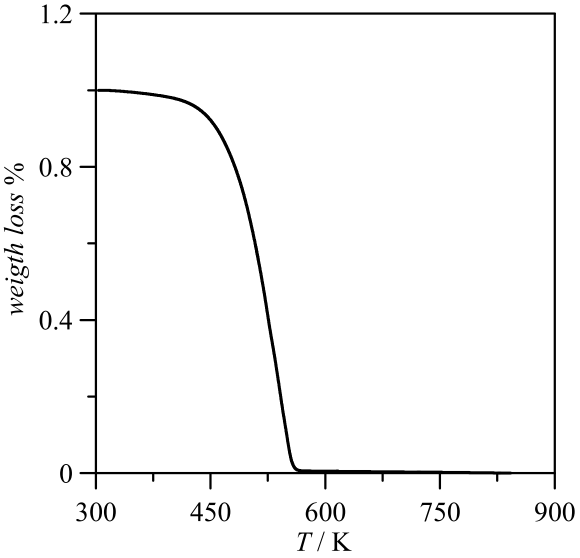

Figure 5.

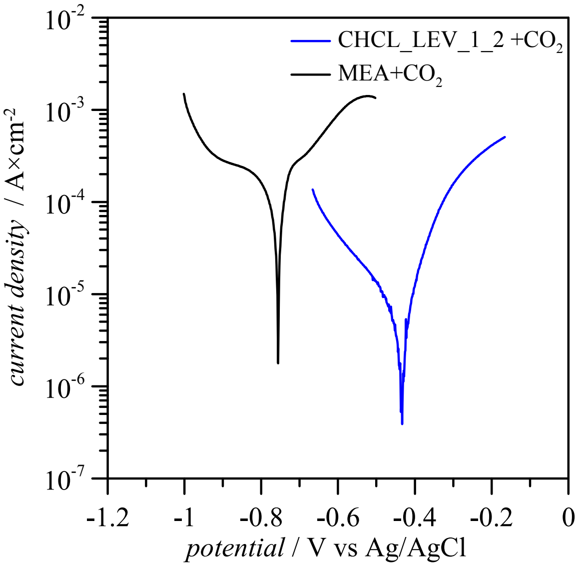
CHCL_LEV_1_2 +CO$_2$
MEA+CO$_2$
current density / A×cm^{-2}
10^{-2}
10^{-3}
10^{-4}
10^{-5}
10^{-6}
10^{-7}
-1.2
-1
-0.8
-0.6
-0.4
-0.2
0
potential / V vs Ag/AgCl

Figure 6.

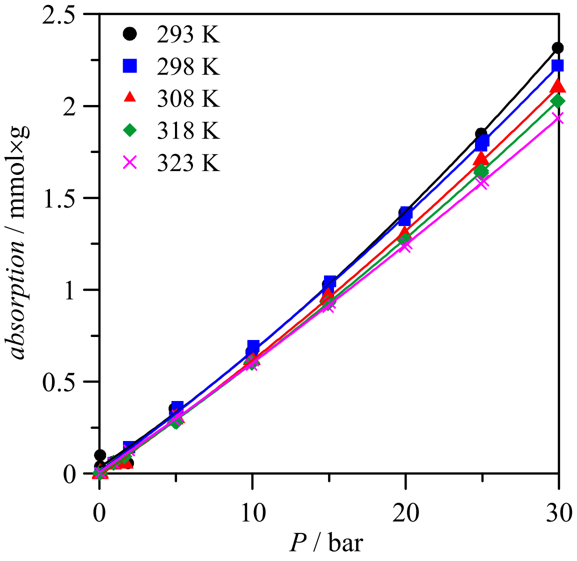

2.5
2
1.5
1
0.5
0
absorption / mmol×g
0
10
20
30
P / bar
● 293 K
■ 298 K
▲ 308 K
◆ 318 K
× 323 K

Figure 7.

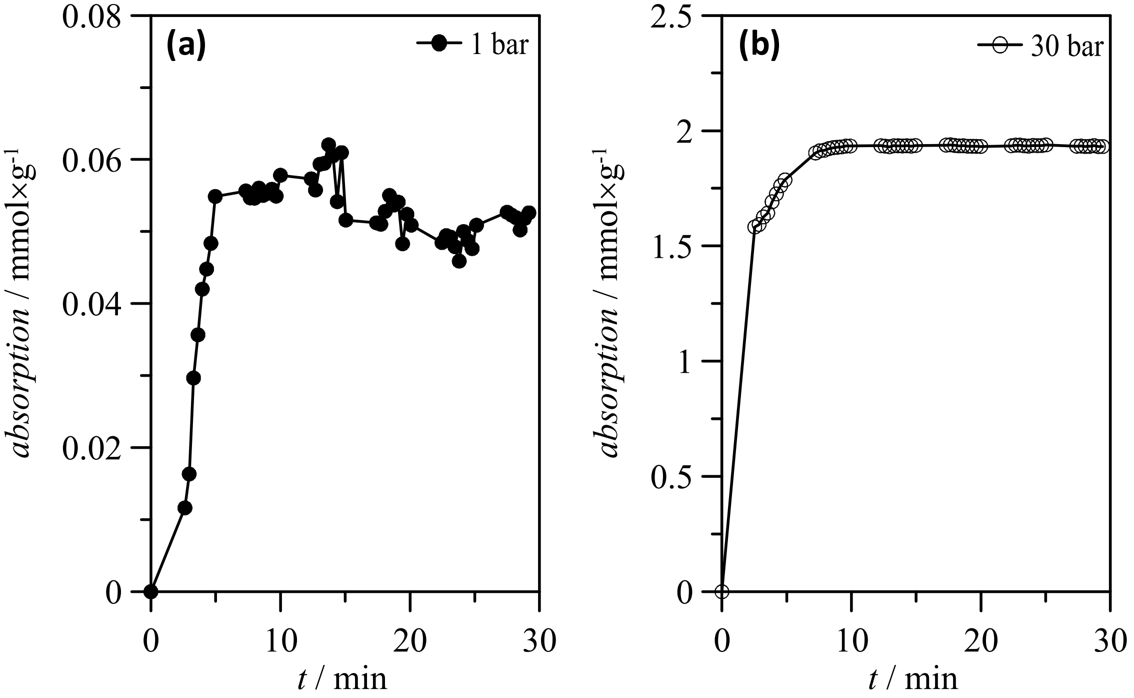
(a)
1 bar
0.08
0.06
0.04
0.02
0
absorption / mmol×g^{-1}
0
10
20
30
t / min
(b)
30 bar
2.5
2
1.5
1
0.5
0
absorption / mmol×g^{-1}
0
10
20
30
t / min

Figure 8.

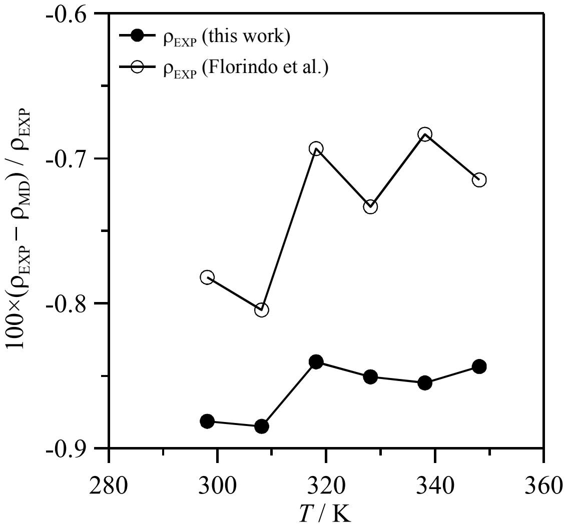
-0.6
-0.7
-0.8
-0.9
280
300
320
340
360
T / K
$100\times(\rho_{EXP}-\rho_{MD})/\rho_{EXP}$
ρ_{EXP} (this work)
ρ_{EXP} (Florindo et al.)

Figure 9.

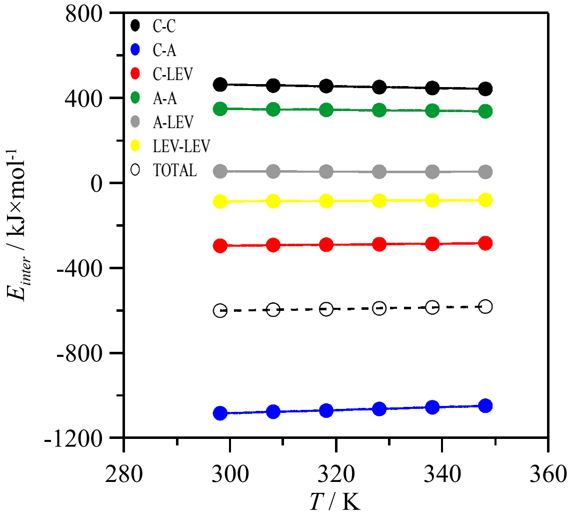
C-C
C-A
C-LEV
A-A
A-LEV
LEV-LEV
TOTAL
800
400
0
-400
-800
-1200
280
300
320
340
360
T / K
E_{inter} / kJ×mol^{-1}

Figure 10.

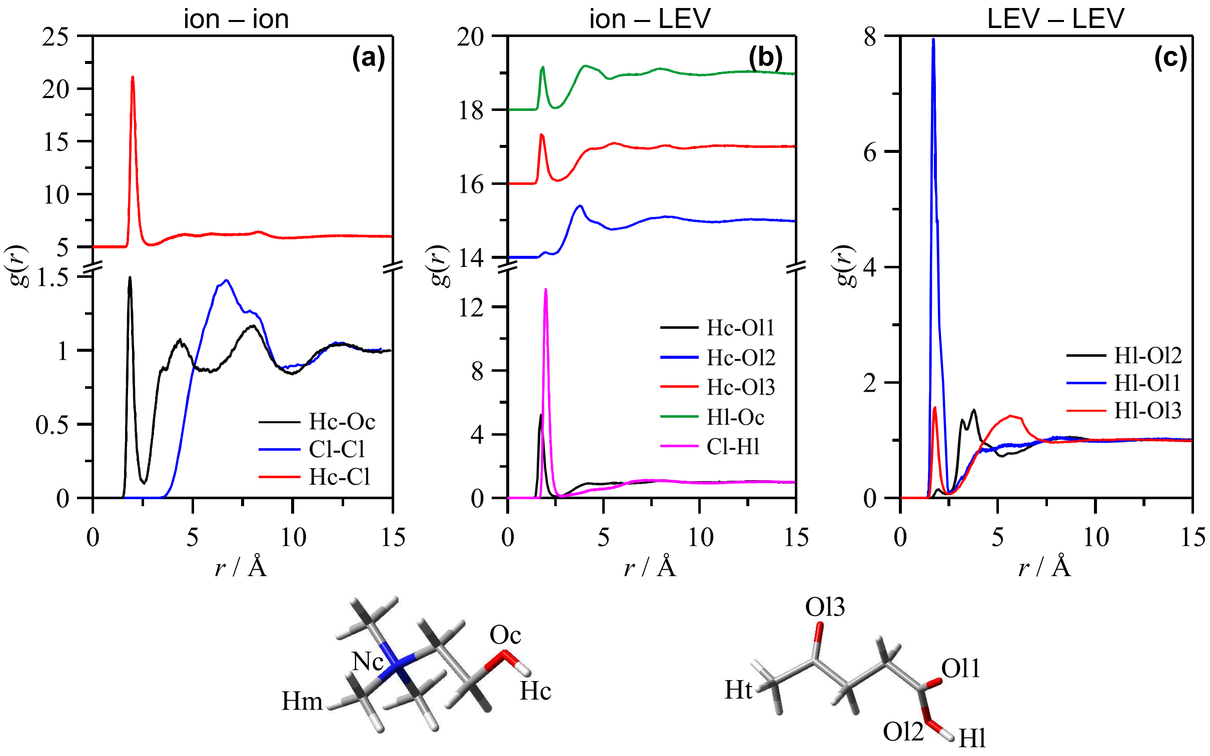
ion – ion
(a)
g(r)
25
20
15
10
5
1.5
1
0.5
0
Hc-Oc
Cl-Cl
Hc-Cl
r / Å
ion – LEV
(b)
20
18
16
14
12
8
4
0
Hc-Ol1
Hc-Ol2
Hc-Ol3
Hl-Oc
Cl-Hl
LEV – LEV
(c)
8
6
4
2
0
Hl-Ol2
Hl-Ol1
Hl-Ol3
0
5
10
15
Nc
Oc
Hc
Hm
Ol3
Ht
Ol1
Ol2
Hl

Figure 11.

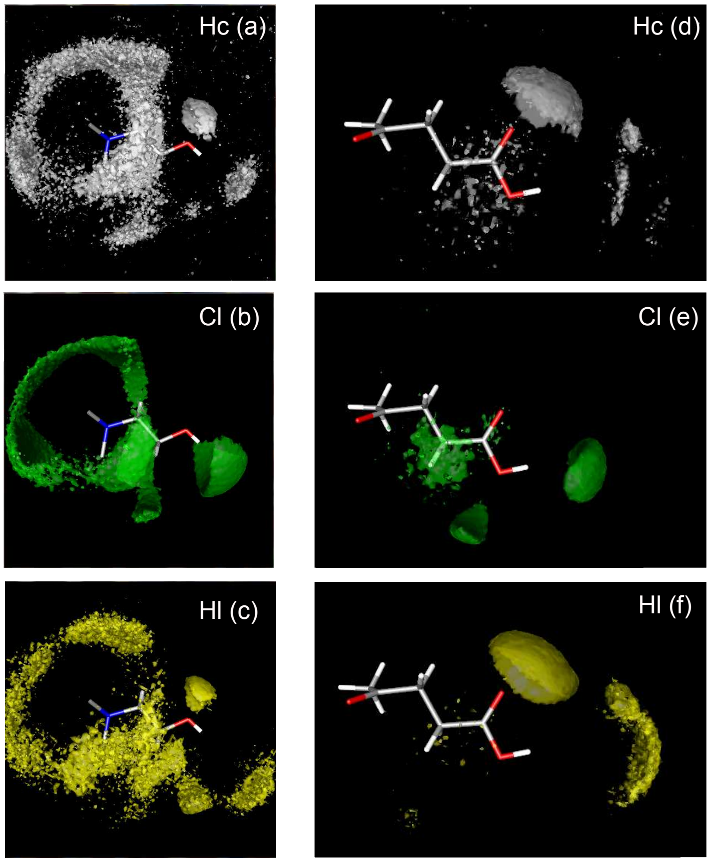

Figure 12.

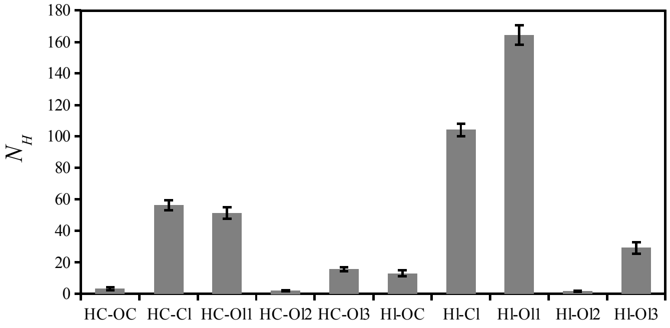
N_H
0
20
40
60
80
100
120
140
160
180
HC-OC
HC-Cl
HC-Ol1
HC-Ol2
HC-Ol3
Hl-OC
Hl-Cl
Hl-Ol1
Hl-Ol2
Hl-Ol3

Figure 13.

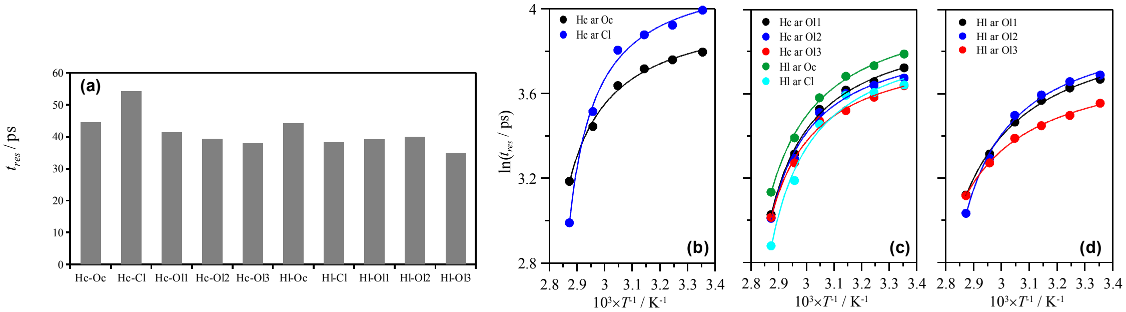
(a)
t_{res} / ps
0
10
20
30
40
50
60
Hc-Oc
Hc-Cl
Hc-Ol1
Hc-Ol2
Hc-Ol3
Hl-Oc
Hl-Cl
Hl-Ol1
Hl-Ol2
Hl-Ol3
(b)
Hc ar Oc
Hc ar Cl
$\ln(t_{res}$ / ps)
2.8
3.2
3.6
4
(c)
Hc ar Ol1
Hc ar Ol2
Hc ar Ol3
Hl ar Oc
Hl ar Cl
(d)
Hl ar Ol1
Hl ar Ol2
Hl ar Ol3
2.8
2.9
3
3.1
3.2
3.3
3.4
$10^3 \times T^{-1}$ / K^{-1}

Figure 14.

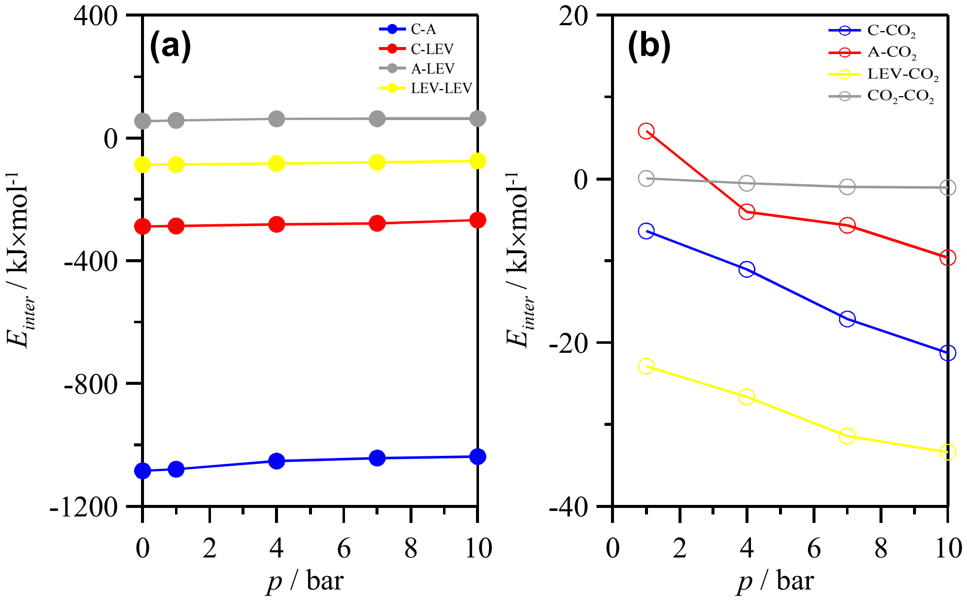
(a)
C-A
C-LEV
A-LEV
LEV-LEV
400
0
-400
-800
-1200
E_{inter} / kJ×mol^{-1}
0
2
4
6
8
10
p / bar
(b)
C-CO$_2$
A-CO$_2$
LEV-CO$_2$
CO$_2$-CO$_2$
20
0
-20
-40
E_{inter} / kJ×mol^{-1}
0
2
4
6
8
10
p / bar

Figure 15.

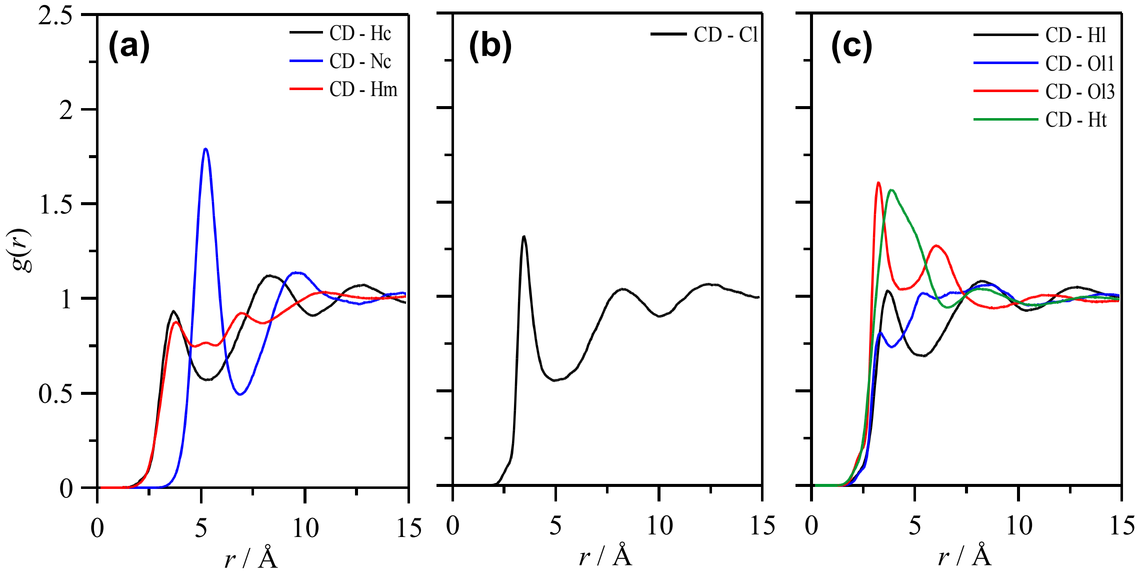
2.5
2
1.5
1
0.5
0
g(r)
(a)
CD - Hc
CD - Nc
CD - Hm
(b)
CD - Cl
(c)
CD - Hl
CD - Ol1
CD - Ol3
CD - Ht
0
5
10
15
r / Å

Figure 16.

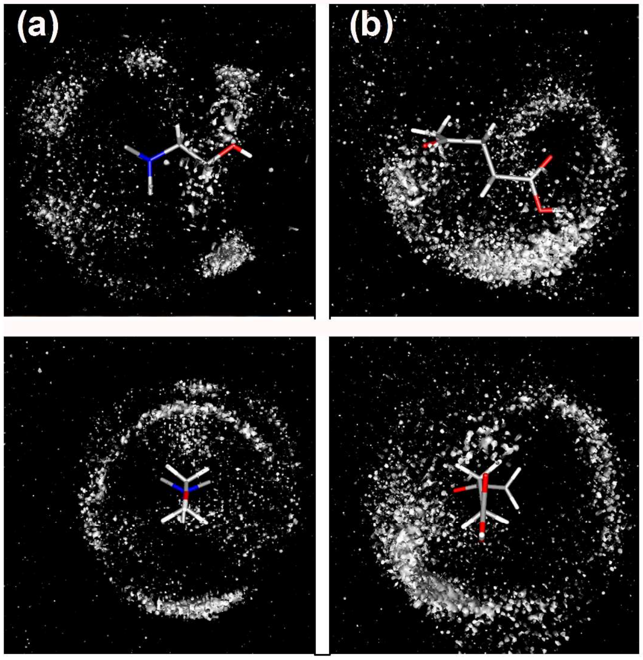

Figure 17.

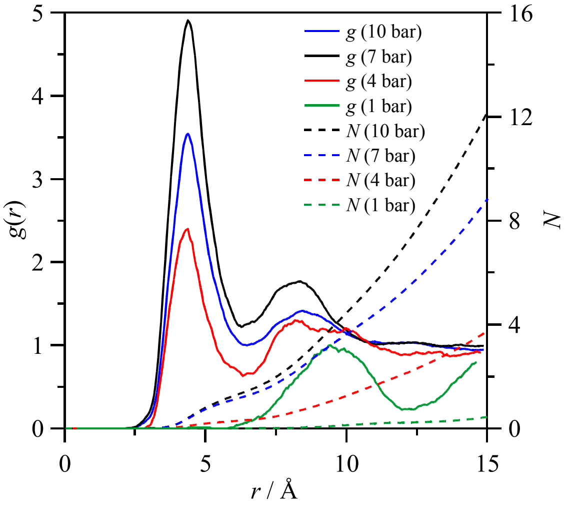
g (10 bar)
g (7 bar)
g (4 bar)
g (1 bar)
N (10 bar)
N (7 bar)
N (4 bar)
N (1 bar)
g(r)
0
1
2
3
4
5
N
0
4
8
12
16
0
5
10
15
r / Å

Figure 18.

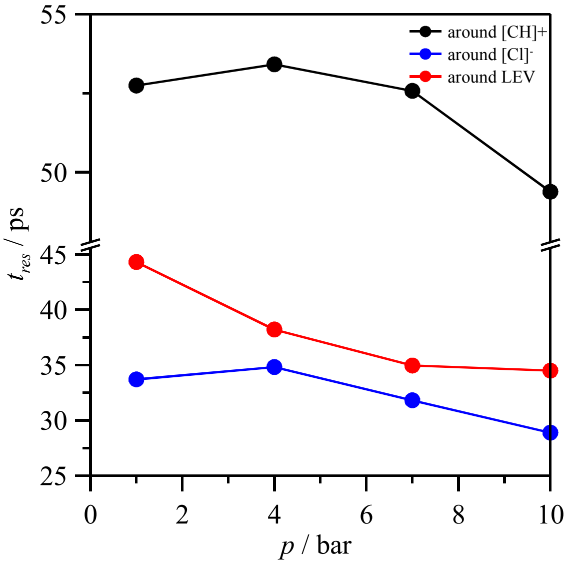
55
50
45
40
35
30
25
0
2
4
6
8
10
t_{res} / ps
p / bar
around [CH]+
around [Cl]⁻
around LEV

Figure 19.

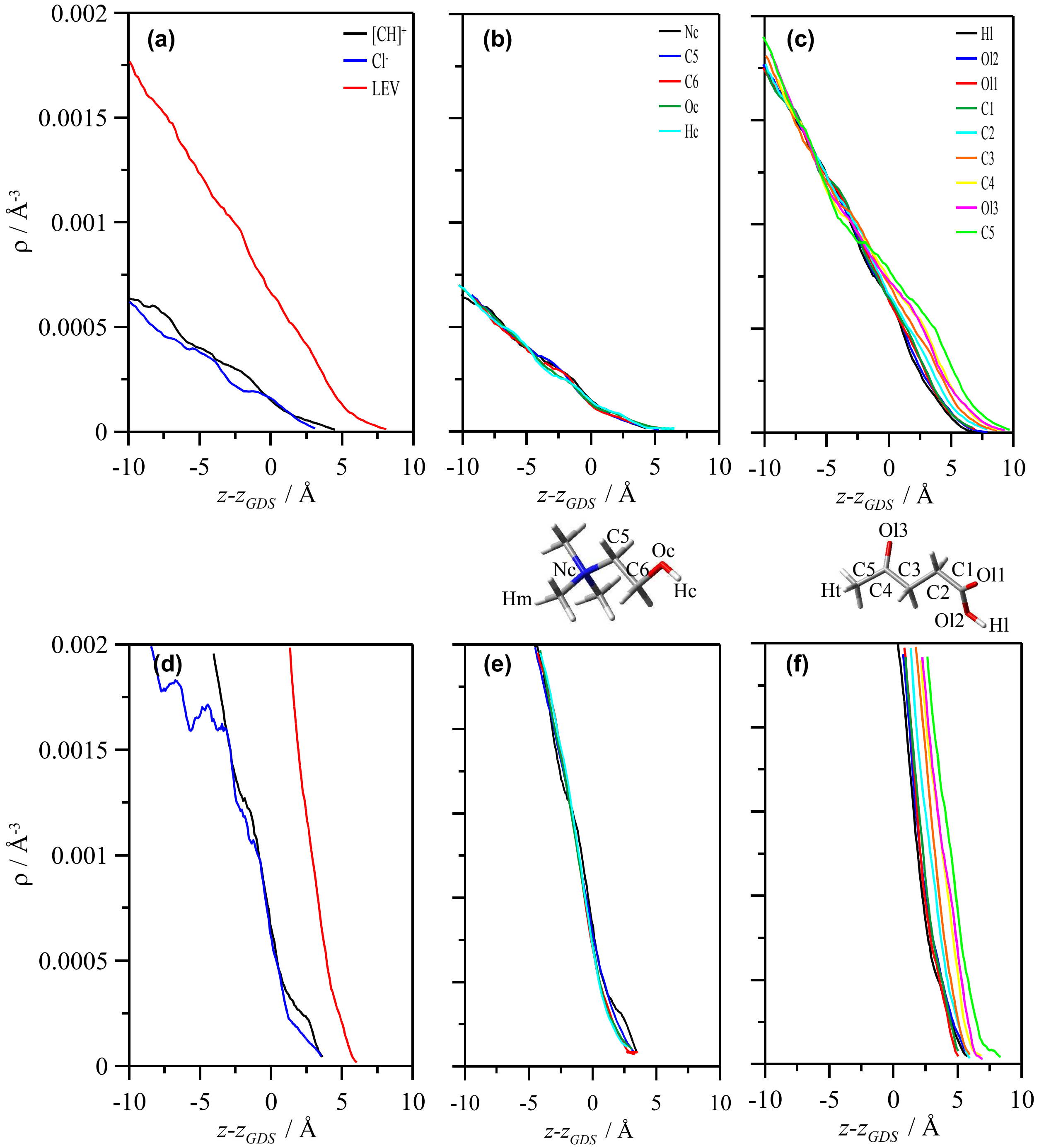
(a)
(b)
(c)
(d)
(e)
(f)
[CH]+
Cl-
LEV
Nc
C5
C6
Oc
Hc
Hl
Ol2
Ol1
C1
C2
C3
C4
Ol3
C5
ρ / Å-3
0.002
0.0015
0.001
0.0005
0
-10
-5
0
5
10
z-zGDS / Å
C5
Oc
Nc
C6
Hm
Hc
Ol3
C5
C3
C1
Ol1
Ht
C4
C2
Ol2
Hl

Figure 20.

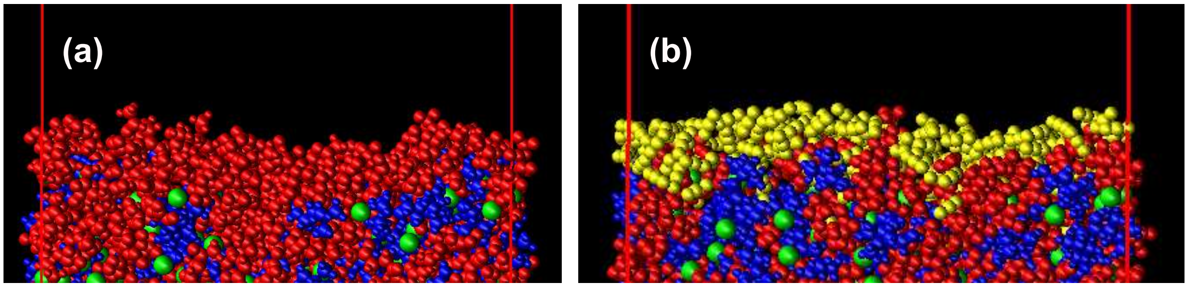

Figure 21.

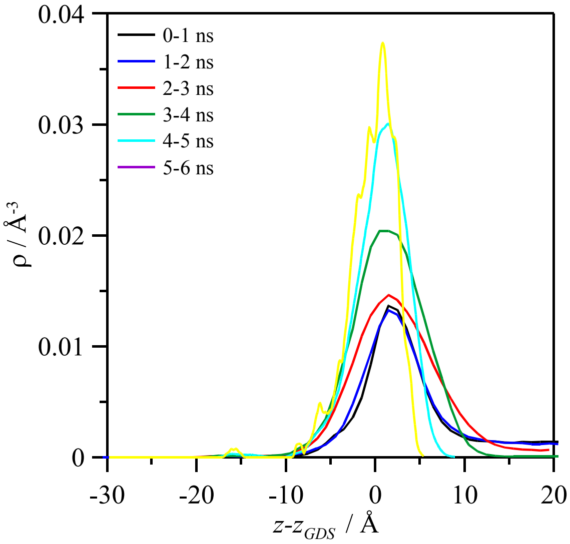
0.04
0.03
0.02
0.01
0
ρ / Å^-3
-30
-20
-10
0
10
20
z-z_GDS / Å
0-1 ns
1-2 ns
2-3 ns
3-4 ns
4-5 ns
5-6 ns

Figure 22.

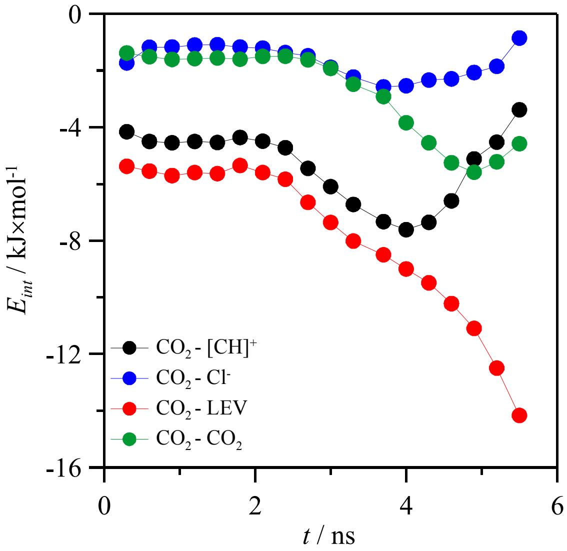

Figure 23.

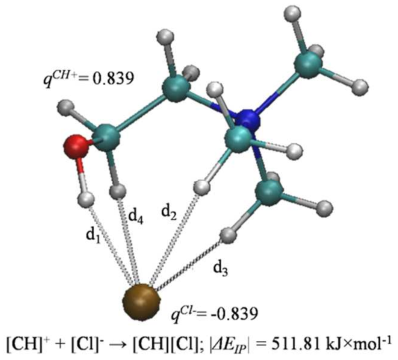
q^{CH+}= 0.839
d_4
d_2
d_1
d_3
q^{Cl-}= -0.839
$[CH]^{+} + [Cl]^{-} \rightarrow [CH][Cl]$; $|\Delta E_{IP}| = 511.81$ kJ×mol^{-1}

Figure 24.

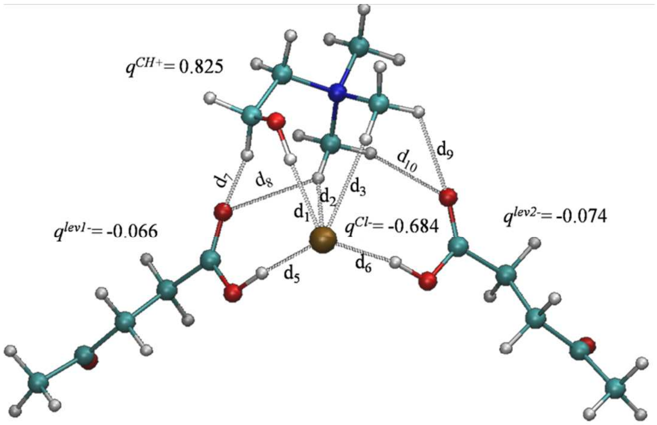

$[CH][Cl]^- + 2\ LEV \rightarrow CHCL\_LEV\_1\_2;\ |\Delta E_{DES}| = 141.93\ kJ \times mol^{-1}$

Figure 25.

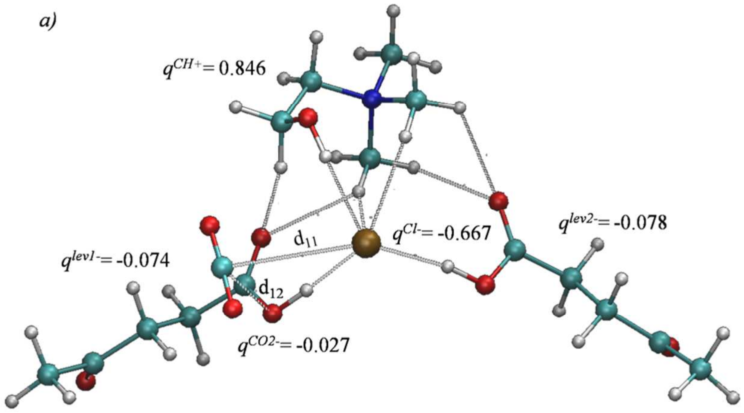

CHCL_LEV_1_2 + CO$_2$→ CHCL_LEV_1_2··· CO$_2$ (a); $|\Delta E_{DES\text{-}CO2}{}^{a}|$ = 17.46 kJ×mol^{-1}

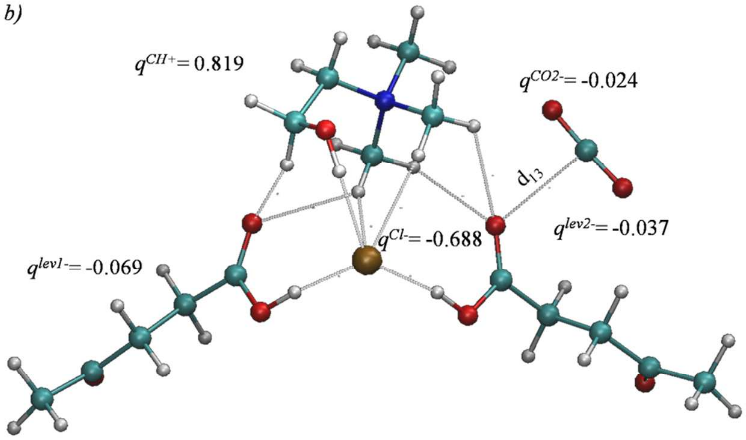

CHCL_LEV_1_2 + CO$_2$→ CHCL_LEV_1_2··· CO$_2$ (b); $|\Delta E_{DES\text{-}CO2}{}^{b}|$ = 24.90 kJ×mol^{-1}

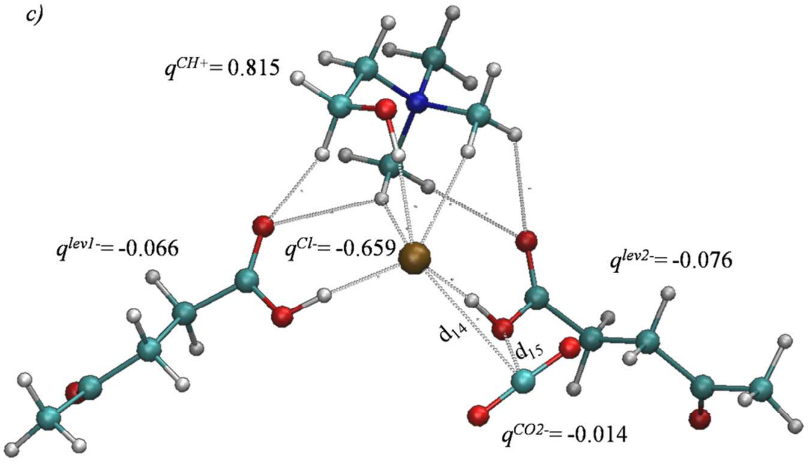

CHCL_LEV_1_2 + CO$_2$→ CHCL_LEV_1_2··· CO$_2$ (c); $|\Delta E_{DES\text{-}CO2}{}^{c}|$ = 14.77 kJ×mol^{-1}

Figure 26.

References

---

1 B. Li, Y. Duan, D. Luebke and B. Morreale, *Appl. Energy*, 2013, 102, 1439-1447.
2 N. von der Assen, J. Jung and A. Bardow, *Energy. Environ. Sci*., 2013, 6, 2721-2734.
3 R. Wennersten, Q. Sun and H. Li, *J. Cleaner Prod*., 2014, DOI: 10.1016/j.jclepro.2014.09.023.
4 M. Kalkuhl, O. Edenhofer and K. Lessman, Environ. Resource. Econ., 2015, 60, 55-80.
5 A. A. Lacis, G. A. Schmidt, D. Rind and R. A. Ruedy, *Science*, 2010, 330, 356-359.
6 P. Fiedlinstein, R. M. Andrew, J. Rogelj, G. P. Peters, J. G. Canadell, R. Knutti, G. Luderer, M. R. Raupach, M. Schaeffer, D. P. van Vuuren and C. Le Quéré, *Nat. Geosci*., 2014, 7, 709-715.
7 T. F. Stocker, D. Qin, G. K. Plattner, M. M. B. Tignor, S. K. Allen, J. Boschung, A. Nauels, Y. Xia, V. Bex and P. M. Midgley, Eds. Climate Change2013: The Physical Science Basis. Contribution of Working Group I to the Fifth Assessment Report of theIntergovernmental Panel on Climate Change. CambridgeUniv. Press, New York, USA 2013.
8 R. L. Revesz, P. H. Hpward, K. Arrow, L. H. Goulder, R. E. Kopp, M. A. Livermore, M. Oppenheimer and T. Sterner, *Nature*, 2014, 508, 173-175.
9 R. S. J. Tol, *Climatic Change*, 2013, 117, 795-808.
10 R. J. Andres, T. A. Boden, F. N. Bréon, P. Ciais, S. Davis, D. Erickson, J. S. Gregg, A. Jacobson, G. Marland, J. T. Miller, T. Oda, J. G. J. Olivier, M. R. Raupach, P. Rayner and K. Treanton, *Biogeosciences*, 2012, 9, 1845-1871.
11 M. Höök and X. Tang, A Review. *Energy Policy*, 2013, 52, 797-809.
12 N. Muradov, Liberating Energy from Carbon: Introduction to Decarbonization. Springer, New York, 2014.
13 S. J. Davis, K. Cladeira and H. D. Matthews, *Science*, 2010, 329, 1330-1333.
14 CO_2 Emissions from Fuel Combustion-2013. International Energy Agency, 2013.
15 Annual Energy Outlook 2014. U.S. Energy Information Administration, Washington, U.S., 2014.
16 World Energy Outlook 2013. International Energy Agency, 2013.
17 C. W. Jones, Chem. Biochem. Eng., 2011, 2, 31-52.
18 G. Luderer, V. Bosetti, M. Jakob, M. Leimbach, J. C. Steckel, H. Waisman and O. Edenhofer, *Climatic Change*, 2012, 114, 9-37.
19 S. J. Friedman, CO_2 Capture and sequestration. In: Fossil Energy. Malhotra R. Ed.. Springer, Menlo Park, CA, USA, 2013, Chapter 16.
20 S. D. Kenarsari, D. Yang, G. Jiang, S. Zhang, J. Wang, A. G. Russell, Q. Wei and M. Fan, *RSC Adv*., 2013, 3, 22739-22773.
21 M. E. Boot-Handford, J. C. Abanades, E. J. Anthony, M. J. Blunt, S.. Brandani, N. Mac Dowell, J. R. Fernández, M. C. Ferrari, R. Gross, J. P. Hallett, R. S. Haszeldine, P. Heptonstal, A. Lyngfelt, Z. Makuch, E. Mangano, R. T. J. Porter, M. Pourkashanian, G. T. Rochelle, N. Shah, J. G. Yao and P. S. Fennell, *Energy Environ. Sci.*, 2014, 7, 130-189.
22 D. Y. C. Leung, G. Caramanna and M. M. Maroto-Valer, Sust. *Energ. Rev*., 2014, 39, 426-443.
23 L. Raynal, P. A. Bouillon, A. Gomez and P. Broutin, *Chem. Eng. J.*, 2011, 171, 742-752.
24 P. Markewitz, W. Kuckshinrichs, W. Leitner, J. Linssen, P. Zapp, R. Bongartz, A. Schreiber and T. E. Müller, *Energy Environ. Sci*., 2012, 5, 7281-7305.
25 V. Scott, S. Gilfillan, N. Markusson, H. Chalmers and R. S. Haszeldine, *Nat. Clim. Change*, 2013, 3, 105-111.
26 G. T. Rochelle, *Science*, 2009, 325, 1652-1654.
27 H. Lepaumier, D. Picq and P. L. Carrette, *Ind. Eng. Chem. Res*., 2009, 48, 9061– 9067.
28 S. Chi and G. T. Rochelle, *Ind. Eng. Chem. Res*., 2002, 41, 4178– 4186.
29 J. Kittel, R. Idem, D. Gelowitz, P. Tontiwachwuthikul, G. Parrain and A. Bonneau, *Energy Procedia*, 2009, 1, 791-797.
30 M. R. M. Abu-Zahra, J. P. M. Niederer, P. H. M. Feron and G. F. Versteeg, *Int. J. Greenh. Gas Con*., 2007, 1, 135-142.
31 L. M. Romeo, I. Bolea and J. M. Escosa, *Appl. Therm. Eng*., 2008, 28, 1039-1046.
32 A. B. Rao and E. S. Rubin, *Environ. Sci. Technol*., 2002, 36, 4467-4475.
33 A. B. Rao and E. S. Rubin, *Ind. Eng. Chem. Res*., 2006, 45, 2421-2429.
34 A. S. Bhown and B. C. Freeman, *Environ. Sci. Technol*., 2011, 45, 8624-8632.
35 J. Husebye, A. L. Brunsvold, S. Roussanaly and X. Zhang,. *Energy Procedia*, 2012, 23, 381-390.
36 K. Sumida, D. L. Rogow, J. A. Mason, T. M. McDonald, E. D. Bloch, Z. R. Herm, T. H. Bae and J. R. Long, *Chem. Rev*., 2012, 112, 724-781.
37 A. Samantha, A. Zhao, G. K. H. Shimizu, P. Sarkar and R. Gupta, *Ind. Eng. Chem. Res*., 2012, 51, 1438-1463.

---

38 M. D. Hornboster, J. Bao, G. Krishnan, A. Nagar, I. Jayaweera, T. Kobayashi, A. Sanjurjo, J. Sweeney, D. Carruthers, M. A. Petruska and L. Dubois, *Carbon*, 2013, 56, 77-85.

39 M. Pera-Titus, *Chem. Rev*., 2014, 114, 1413-1492.

40 F. Karadas, M. Atilhan and S. Aparicio, *Energy Fuel.*, 2010, 24, 5817-5828.

41 X. Zhang, X. Zhang, H. Dong, Z. Zhao, S. Zhang and Y. Huang, *Energy Environ. Sci*., 2012, 5, 6668-6681.

42 M. Ramdin, T. W. de Loos and T. J. H. Vlugt, *Ind. Eng. Chem. Res*., 2012, 51, 8149-8177.

43 R. Biczak, B. Pawlowska and P. Balczewski *J. Hazard. Mater*., 2014, 274, 181-190.

44 T. P. N. Pham, C. W. Cho and Y. S. Yun, *Water Res*., 2010, 44, 352-372.

45 B. Peric, J. Sierra, E. Martí, R. Cruañas, M. A.. Garau, J. Arning, U. Bottin-Weber and S. Stolte, *J. Hazard. Mater*., 2013, 261, 99-105.

46 M. Smiglak, W. M. Reichert, J. D. Holbrey, J. S. Wilkes, L.. Sun, J. S. Thrasher, K.. Kirichenko, S. Singh A. R. Katritzky and R. D. Rogers, *Chem. Commun*., 2006, 2554-2556.

47 K. Paduszynski and U. Dománska, *J. Chem. Inf. Model*., 2014, 54, 1311-1324.

48 L. Chen, M. Sharifzadeh, N. MacDowell, T. Welton, N. Shah and J. P. Hallett, *Green Chem*., 2014, 16, 3098-3106.

49 M. Petkovic, K. R. Seddon, L. P. N. Rebelo and C. Silva-Pereira, *Chem. Soc. Rev*., 2011, 40, 1383-1403.

50 S. P. M. Ventura, F. Silva, A. M. M. Goncalves, J. L. Pereira, F. Goncalves and J. A. P. Coutinho, *Ecotox. Environ. Safe.*, 2014, 102, 48-54.

51 X. D. Hou, Q. P. Liu, T. J. Smith, N. Li and M. H. Zong, *PLOS One*, 2013, 8, e59145.

52 C. Asumana, G. Yu, X. Li, J. Zhao, G. Liu and X. Chen, *Green Chem*., 2010, 12, 2030-2037.

53 A. Paiva, R. Caraverio, I. Aroso, M. Martins, R. L. Reis and A. R. C. Duarte, *ACS Sus. Chem. Eng*., 2014, 2, 1063-1071.

54 Q. Zhang, K. O. Vigier, S. Royer and F. Jérôme, *Chem. Soc. Rev*., 2012, 41, 7108-7146.

55 H. G. Morrison, C. C. Sun and S. Neervannan, *Int. J. Pharm*., 2009, 378, 136-139.

56 B. S. Singh, H. R. Lobo and G. S. Shankarling, *Catal. Commun*., 2012, 24, 70-74.

57 Y. H. Choi, J. van Spronsen, Y. T. Dai, M. Vermerne, F. Hollmann, I. W. C. E. Arends, G. J. Witkamp and R. Verpoorte, *Plant. Physiol*., 2011, 156, 1701-1705.

58 Y. Dai, J. van Spronsen, G. J. Witkamp, R. Verpoorte and Y. H. Choi, Anal. Chim. Acta, 2013, 766, 61-68.

59 Z. Maugeri and P. Domínguez, *RSC Adv*., 2012, 2, 421-425.

60 C. Florindo, F. S. Oliveira, L. P. N. Rebelo, A. M. Fernandes and I. M. Marrucho, *ACS Sus. Chem. Eng*., 2014, 2, 2416-2425.

61 J. Bozell, L.. Moens, D. C. Elliott, Y. Wang, G. G. Neuenscwander, S. W. Fitzpatrick, R. J. Bilski and J. L. Jarnefeld, *Resourc. Conser. Rec*., 2000, 28, 227-239.

62 C. Chang, P. Cen and X. Ma, *Biores. Tech*., 2007, 98, 1448-1453.

63 R. Weingartner, W. C. Conner and G. W. Huber, *Energy Environ. Sci.*, 2012, 5, 7559-7574.

64 X. Li, M. Hou, B. Han, X. Wang and L. Zou, *J. Chem. Eng. Data*, 2008, 53, 548-550.

65 R. B. Leron, A. Caparanga and M. L. Li, *J. Taiwan Inst. Chem. Eng.*, 2013, 44, 879-885.

66 R. B. Leron and M. H. Li, *Thermochim. Acta*, 2013, 551, 14-19.

67 R. B. Leron and M. H. Li, *J. Chem. Thermodyn*., 2013, 57, 131-136.

68 M. Francisco, A. van den Bruinhorst, L. F. Zubeir, C. J. Petersand M. C. Kroon, *Fluid Phase Equilibr*., 2013, 340, 77-84.

69 Y. C. Chen, N. Ai, H. Shan, Y. Cui and D. Deng, *J. Chem. Eng. Data*, 2014, 59, 1247-1253.

70 C. M., R. B. Leron, A. R. Caparanga and M. H. Li, *J. Chem. Thermodyn*., 2014, 68, 216-220.

71 Y. Chen, N. Ai, H. Shan, Y. Cui and D. Deng, *J. Chem. Eng. Data*, 2014, 59, 1247-1253.

72 G. Li, D. Deng, Y. Chen,. H. Shan and N. Ai, *J. Chem. Thermodyn*., 2014, 75, 58-62.

73 P. Hapiot and C. Lagrost, *Chem. Rev*., 2008, 108, 2238-2264.

74 A. P. Abbott, D. Boothby, G. Capper, D. L. Davies and R. K. Rasheed, *J. Am. Chem. Soc*., 2004, 126, 9142-9147.

75 ASTM Standard G1-03. Standard Practice for Preparing, Cleaning and Evaluating Corrosion Test Specimens. In: Annual Book of ASTM Standards American Society of Testing Materials: West Conshohcken, PA, 2003.

76 F. Karadas, C. T. Yavuz, S. Zulfiqar, S. Aparicio, G. D. Stucky, M. Atilhan, *Langmuir*, 2011, 27, 10642-10647.

77 D. E. Cristancho, I. D. Mantilla, S. Ejaz, K. R. Hall, G. A. Iglesias-Silva and M.. Atilhan, *Int. J. Thermophys*., 2009, 31, 698-709.

78 C. Lee, W. Yang, R. G. Parr, *Phys. Rev. B*, 1988, 37, 785-789; A. D. Becke, *J. Chem. Phys*., 1993, 98,5648 – 5652.

79 A. D. Becke, *Phys. Rev. A*, 1988, 38, 3098-3100.

80 S. Grimme, *J. Comput. Chem*., 2006,27, 1787-1799.

---

81 A. J. Cohen, P. Mori-Sánchez and W. Yang, *Chem. Rev*., 2012, 112, 289-320.
82 T. Schwabe and S. Grimme, *Phys. Chem. Chem. Phys*., 2007, 9, 3397-3406.
83 S. Simon, M. Duran and J. J. Dannenberg, *J. Chem. Phys*., 1996, 105, 11024.
84 R. F. W. Bader, Atoms in Molecules: a Quantum Theory. Oxford, 1990.
85 T. Lu and F. J. Chen, *J. Comput. Chem*., 2012, 33, 580-592.
86 C. M. Breneman and K. B. Wiberg, J. Comput. Chem., 1990, 11, 361-373.
87 M. J. Frisch, G. W. Trucks, H. B. Schlegel, G. E. Scuseria, M. A. Robb, J. R. Cheeseman, G. Scalmani, V. Barone, B. Mennucci, G. A. Petersson, H. Nakatsuji, M. Caricato, X. Li, H. P. Hratchian, A. F. Izmaylov, J. Bloino, G. Zheng, J. L. Sonnenberg, M. Hada, M. Ehara, K. Toyota, R. Fukuda, J. Hasegawa, M. Ishida, T. Nakajima, Y. Honda, O. Kitao, H. Nakai, T. Vreven, J. A. Montgomery, Jr., J. E. Peralta, F. Ogliaro, M. Bearpark, J. J. Heyd, E. Brothers, K. N. Kudin, V. N. Staroverov, R. Kobayashi, J. Normand, K. Raghavachari, A. Rendell, J. C. Burant, S. S. Iyengar, J. Tomasi, M. Cossi, N. Rega, J. M. Millam, M. Klene, J. E. Knox, J. B. Cross, V. Bakken, C. Adamo, J. Jaramillo, R. Gomperts, R. E. Stratmann, O. Yazyev, A. J. Austin, R. Cammi, C. Pomelli, J. W. Ochterski, R. L. Martin, K. Morokuma, V. G. Zakrzewski, G. A. Voth, P. Salvador, J. J. Dannenberg, S. Dapprich, A. D. Daniels, Ö. Farkas, J. B. Foresman, J. V. Ortiz, J. Cioslowski, and D. J. Fox. Gaussian 09, Revision **D.01**, Gaussian, Inc.: Wallingford, CT, USA, 2009.
88 L. Martínez, R. Andrade, E. G. Birgin and J.M. Martínez, *J. Comput. Chem*., 2009, 30, 2157-2164.
89 E. W. Lemmon, M. L. Huber and M. O. McLinden, NIST Standard Reference Database 23: Reference Fluid Thermodynamic and Transport Properties-REFPROP, Version 9.1, National Institute of Standards and Technology, Standard Reference Data Program, Gaithersburg, 2013.
90 A. P. Lyubartsev and A. Laaksonen, *Comput. Phys. Commun*., 2000, 128, 565-589.
91 U. L. Essmann, M. L. Perera, T. Berkowitz, H. Darden, H. Lee and L. G. Pedersen, *J. Chem. Phys*., 1995, 103, 8577-8593.
92 M. Tuckerman, B. J. Berne and G. J. Martyna, *J. Chem. Phys*., 1992, 97, 1990-2001.
93 W. Guo, Y. Hou, S. Ren, S. Tian and W.. Wu, *J. Chem. Eng. Dat*a, 2013, 58, 866-872.
94 C. D'Agostino, R. C. Harris, A. P. Abbott, L. F. Gladden and M. D. Mantle, *Phys. Chem. Chem. Phys*., 2011, 13, 21383-21391.
95 A. Yadav, S. Trivedi, R. Rai and S. Pandey, *Fluid Phase Equilibr*., 2014, 367, 135-142.
96 G. García, S. Aparicio, R. Ullah, M. Atilhan, *Energy Fuel*., 2015, in press, DOI: 10.1021/ef5028873.
97 A. Abbott, E. I. Ahmed, R. C. Harris and K. S. Ryder, *Green Chem*., 2014, 16, 4156−4161.
98 E.W. Lemmon, M.L. Huber and M.O. McLinden, NIST Reference Fluid Thermodynamic and Transport Properties REFPROP, Version 8.0; National Institute of Standards and Technology, Standard Reference Data Program: Gaithersburg, MD, 2007.
99 S. L. Perkins, P. Painter and C. M. Colina, *J. Phys. Chem. B*, 2013, 117, 10250-10260.
100 S. P. Verevkin, D. H. Zaitsau, V. N. Emel'yanenko, A. V. Yermalayeu, C. Schick, H. Liu, E. J. Maginn, S. Bulut, I. Krossing and R. Kalb, *J. Phys. Chem. B*, 2013, 117, 6473-6486.
101 Y. Zhang and E. J. Maginn, *Phys. Chem. Chem. Phys*., 2014, 16, 13489-134999.
102 H. Sun,Y. Li and G. Li, *J. Mol. Model*., 2013, 19, 2433-2441.
103 G. García, J. L. Trenzado, R. Alcalde, A. Rodriguez-Delgado, M. Atilhan and S. Aparicio, S. *J. Phys. Chem. B*, 2014, 118, 11310-11 322.